Controlling the Dual Cascade of Two-dimensional Turbulence

Controlling the Dual Cascade of Two-dimensional Turbulence

By
MOHAMMAD M. FARAZMAND, B.Sc.

A Thesis
Submitted to the School of Graduate Studies
in Partial Fulfilment of the Requirements
for the Degree
Master of Applied Science

McMaster University

MASTER OF APPLIED SCIENCE (2010) McMaster University
(Computational Engineering and Science) Hamilton, Ontario

TITLE:	Controlling the Dual Cascade of Two-dimensional Turbulence
AUTHOR:	Mohammad M. Farazmand, B.Sc. (Sharif University of Tech)
SUPERVISORS:	Nicholas Kevlahan
NUMBER OF PAGES:	vi, 61

Abstract

The Kraichnan–Leith-Batchelor (KLB) theory of statistically stationary forced homogeneous isotropic 2-D turbulence predicts the existence of two inertial ranges: an energy inertial range with an energy spectrum scaling of $k^{-5/3}$, and an enstrophy inertial range with an energy spectrum scaling of k^{-3}. However, unlike the analogous Kolmogorov theory for 3-D turbulence, the scaling of the enstrophy range in 2-D turbulence seems to be Reynolds number dependent: numerical simulations have shown that as Reynolds number tends to infinity the enstrophy range of the energy spectrum converges to the KLB prediction, i.e. $E \sim k^{-3}$.

We develop an adjoint-equation based optimal control approach for controlling the energy spectrum of incompressible fluid flow. The equations are solved numerically by a highly accurate method. The computations are carried out on parallel computers in order to achieve a reasonable computational time.

The results show that the time-space structure of the forcing can significantly alter the scaling of the energy spectrum over inertial ranges. This effect has been neglected in most previous numerical simulations by using a random-phase forcing. A careful analysis of the resulting forcing suggests that it is unlikely to be realized in nature, or by a simple numerical model. Therefore, we conjecture that the dual cascade is unlikely to be realizable at moderate Reynolds numbers without resorting to forcings that depend on the instantaneous flow structure or are not band-limited.

Acknowledgements

I would like to sincerely thank my supervisor Prof. Nicholas Kevlahan to whom I owe a lot for his invaluable encouragement, supervision and support. I express my profound gratitude to Dr. Bartosz Protas for his generous help with the optimal control method and all his friendly advice throughout my Masters studies. In addition, my thanks to the professors who lectured me during my course work: Professors Antoin Deza, Ned Nedialkov, Lia Bronsard and Jean P. Gabardo.

McMaster University deserves many thanks for providing a wonderful research environment. In particular, I thank all members of the Applied and Industrial Mathematics (AIMS) lab at the department of Mathematics and Statistics for all their friendly help and discussions. Special thanks to Prof. Walter Craig and Prof. Dmitry Pelinovsky for their instructive comments and constructive criticism during the AIMS lab meetings.

The numerical simulations of this project were carried out by the facilities of the Shared Hierarchical Academic Research Computing Network (SHARCNET) without which the completion of this research would be impossible.

Contents

Chapter 1

Introduction

1.1 Introduction

Turbulence in fluids is *naively* refered to a complicated fluid motion which arises in high speed flow over large length scales. Since there are no universal theory of turbulence, there is no widely accepted definition of turbulent flow. In spite of this lack of definition, there are many example of flows which are called turbulent. Most of fluid flows in nature such as atmospheric flow, oceanic flow and flow of the liquid core of the earth are turbulent. All these flows share some features. Firstly, they consist of various scales of motion with entangled dynamics. The energy is being constantly transfered among these scales in a rather complicated way (see §2.2). Even if the initial state of the flow includes a few scales of motion, gradually more and more scales will come into play and turn the initially simple flow into a complicated turbulent flow. This is illustrated in figure 1.1 by the energy of different scales of motion as time increases. Secondly, the dynamics of these flows are quite non-local in the sence that a change in a particular point of the flow can affect the flow far away from that point. This strong correlation exists in time too.

On the other hand, the mathematical equations which describe turbulent flows are complicated (see §2.1). There are generally no analytic solutions to these equations. Even the property analysis of the possible solutions is very difficult in most cases. Being computationally expensive, direct numerical solution of these equations are feasible only for relatively small problems with simple geometries (see §3.2). These complexities have embeded our understanding of turbulence. However, under some simplifying assumptions, one can make some predictions about the statistical properties of turbulent flows.

In 1941 Kolmogorov proposed a statistical theory for homogeneous, isotropic and statistically stationary[1] three-dimensional incompressible turbulence [17]. He assumed that there is an inertial range of length scales in which the effect

[1]For the definitions of isotropy, homogenuity and statistical stationarity, the reader can refer to §2.4.

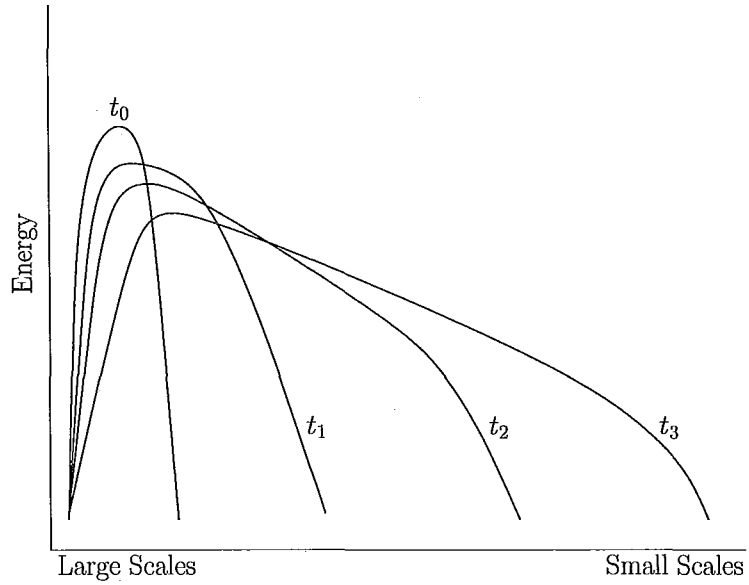

Figure 1.1: The qualitative behavior of the energy spectrum in a turnulent flow. It illustrates that smaller and smaller sclaes of motion come into play as time increases. The variables $t_0 < t_1 < t_2 < t_3$ denote the time. This figures corresponds to 3-D turbulence. The case of 2-D turbulence is different in details as described below.

of the external forcing and the molecular viscosity are negligible. Since in the inertial range the energy spectrum, $E(k)$, depends only on the mean energy dissipation rate ϵ and the wavenumber k, dimensional analysis shows that the energy spectrum must follow the universal form:

$$E(k) = C\epsilon^{2/3}k^{-5/3} \tag{1.1}$$

where C is a universal constant. Moreover, he conjectured that in three dimensions the turbulent energy is transferred from larger scales (lower wavenumbers) to smaller scales (higher wavenumbers) where the energy is eventually dissipated by viscosity. The $k^{-5/3}$ prediction has been verified to high accuracy in numerous experiments and computations (apart from small corrections due to the intermittency of the energy dissipation rate).

The success and simplicity of Kolmogorov's theory has inspired efforts to adapt the theory to two-dimensional turbulence. In spite of the fact that there are no truly two-dimensional flows in nature, it is believed to be a good approximation for flows in which one lengthscale is much smaller than the other two, e.g. large scale flow in the atmosphere and oceans [11]. However, Kolmogorov's theory does not apply directly to two-dimensional flow since the dynamics of two-dimensional flows are qualitatively different from three-dimensional flows. For example, vortex stretching which plays a key role in energy transfer between scales in 3-D is absent in 2-D. In addition, Fjørtoft [9] (and later Merilees

and Warn [26] and Gkioulekas and Tung [15]) showed that in a 2-D incompressible Navier–Stokes flow the energy is (on average) transferred to larger scales, while the enstrophy is transferred to smaller scales. This so-called *dual cascade* is quite different from the 3-D case where the energy cascades down to smaller scales in the inertial range. Based on Fjørtoft's work and Kolmogorov's universality assumption, Kraichnan [18], Leith [20] and Batchelor [2] developed an analogous theory (usually referred to as KLB theory) for homogeneous, isotropic and statistically stationary two-dimensional forced turbulence.

According to the KLB theory, in 2-D Navier–Stokes turbulence, there are two inertial ranges (of energy and enstrophy[2] respectively) where the effects of the viscosity and the external forces are negligible. The energy and the enstrophy are injected by external forcing in some intermediate scales between energy and enstrophy inertial ranges. The injected energy is then transferred to ever larger scales through the energy inertial range while the enstrophy is transferred to smaller scales through the enstrophy inertial range until it is eventually dissipated by molecular viscosity. Kraichnan assumed that in the energy inertial range the energy spectrum of the flow, $E(k)$, depends only on the energy dissipation rate (ϵ) and the wavenumber k, while, in the enstrophy inertial range, $E(k)$ depends only on enstrophy dissipation rate (η) and k. Using dimensional analysis, he then predicted the following scaling laws: $E(k) \propto k^{-5/3}$ in the energy inertial range (just as in three-dimensional turbulence) and $E(k) \propto k^{-3}$ (with a possible logarithmic correction [see 19]) in the enstrophy inertial range (see figure 2.5 for an illustration).

Many numerical and laboratory experiments have been performed in attempts to test the KLB theory [see, for instance, 21, 28, 3]. These experiments confirm the general setting of the theory. Each of the cascades have been observed *independently* with the predicted slopes. However, there is a controversy. KLB theory predicts that if enough energy and enstrophy are injected into the system these dual cascades (i.e. inverse cascade of energy and forward cascade of enstrophy) must be realizable *simultaneously* in a statistically stationary state. (Indeed, the inverse cascade of energy can be only quasi-stationary in an infinite domain since the energy is transferred to ever larger scales.) In the numerical and experimental studies, which attempt to realize the dual cascades of 2-D turbulence simultaneously, the $-5/3$ slope of the inverse cascade has been well established [see 33, 12], however, slopes significantly steeper than -3 have been found for the forward cascade. To the best of our knowledge, Boffetta [3] presents the closest result to the KLB prediction. At the highest Reynolds number (i.e. a resolution of 16384^2) their enstrophy cascade exhibits a slope of (almost) -3.8.

Some attempts have been made to explain this departure from the KLB the-

[2]Enstrophy is squared vorticity.

ory. First, it should be noted that while the KLB theory assumes unbounded domains the numerical and laboratory experiments are necessarily performed on bounded domains. Kraichnan [18] pointed out from the very beginning that this may affect the results of the experiments since the energy transferred by the inverse cascade accumulates in the largest available scales. This problem is avoided by adding a friction-type dissipation to remove energy at the largest scales. This type of dissipation, usually called Rayleigh friction (or Ekman drag), is natural in atmospheric flow because of the friction between flow and the earth's surface [1]. On the other hand, Tran and Dritschel [35] [also see 37] disproved one of the underlying assumption of KLB theory: that enstrophy dissipation converges to a non-zero value in the zero molecular viscosity limit. (This prediction is the analogue of the prediction that energy dissipation rate converges to a non-zero finite value as Reynolds number tends to infinity in three-dimensional turbulence.) However, Tran et al. [37] showed (by substituting enstrophy dissipation with a Reynolds dependent quantity) that the -3 slope of the enstrophy cascade should still hold.

Another question which is still not well understood is the effect of the forcing on the dual cascades in forced–dissipative two-dimensional turbulence. Studies have shown that the type of forcing modifies the slope of the enstrophy inertial range spectrum. The convention is that a monoscale or a monoscale-like (band-limited) forcing is used. The forcing is confined to a single wave number in the case of monoscale forcing, or to a few adjacent wavenumbers in the monoscale-like case. The input energy is transferred to larger scales and the input enstrophy to the smaller scales as predicted by KLB. This type of forcing, first suggested by [18], has some advantages. First, it is easy to control the rate of energy and enstrophy injection and secondly, the energy and enstrophy injection ranges do not overlap with the inertial ranges. It is also consistent with the inertial range hypothesis, that conjectures that the energy input is negligible in the inertial ranges.

However, in 1994 Constantin et al. [7] proved that, in a finite domain, monoscale forcing cannot produce dual cascades with the slopes predicted by KLB. Later, Tran and Shepherd [36] and Tran and Bowman [34] generalized this result to band-limited forcing and more general types of dissipation. They proved that with monoscale (or monoscale-like) forcing, the slope of the energy spectrum in the forward cascade *cannot* be shallower than -5. These results show that monoscale and monoscale-like forcing are actually inconsistent with KLB theory. Tran and Shepherd [36] showed that in the presence of inverse viscosity (which removes energy from large scales) the KLB scaling is theoretically possible. However, as was mentioned before, this result suffers lack of numerical and experimental evidence.

On the other hand, Lundgren [23] proposed a linear forcing (directly pro-

portional to the velocity) to study three-dimensional turbulence. Lundgren was motivated by the need to find a forcing that has a better physical justification and easier to apply in non-spectral simulations than the usual spectral forcing applied only to a few small wavenumbers. Later, [30] further studied the effects of this type of forcing. Their results show that the predictions of the Kolmogorov theory still hold under linear forcing, despite the fact that linear forcing is active at all scales.

In two dimensions, the effects of linear damping which is active in all scales (as opposed to Rayleigh friction which is active only at the largest scales) has been studied in recent years [4, 39, 38]. It should be noted that both linear forcing and linear damping are active over all scales, including the energy and enstrophy *inertial* ranges. This appears to violate the inertial range hypothesis because energy is added (removed) directly at (from) all scales. However, the above mentioned studies show that the energy flux (and enstrophy flux in 2-D case) remains almost constant over a wide range of wavenumbers, even when linear forcing or damping is applied. These observations raises the question of whether there are types of forcing (possibly active at all scales) which are able to produce the dual cascades with the scaling laws predicted by KLB theory. Answering this question is one of the goals of the present paper.

The other goal is to investigate the effect of the space-time structure of the band-limited forcing on the energy spectrum. In most previous numerical simulations, the forcing is random in phase [see e.g. 31]. In some simulations, the forcing is delta-correlated in time [see e.g. 3]. In some others, the time correlation is increased by a Markov process [see e.g. 21]. There are also simulations in which the forcing depends on the instantaneous velocity field [see e.g. 6]. The motivation for using each of these forcings is to have a control on the energy and enstrophy injection rates. Therefore, there is no unique and physically well-justified way to define the forcing. Almost always, the effect of the space-time structure of the forcing on the energy spectrum is neglected. Here, we show that the details of this space-time structure can have determining effects on the slopes of the cascades even when the forcing is band-limited.

The rest of the thesis is organized as follows. In chapter 2 the governing equations and the basic concepts of 2-D turbulence are presented. Chapter 3 starts with our formulation of the control problem and continues with the some remarks about the compuational method we use to solve the equations. In chapter 4, the results of the application of the control method to the 2-D turbulence problem are presented and discussed. In the last chapter we present the conclusions and some future directions.

Chapter 2

Theory of Two-dimensional Turbulence

In this chapter we review the basic equations and concepts related to the two-dimensional turbulence. First we state the incompressible Navier-Stokes equations (NSE) in physical and Fourier spaces. The vorticity equations are also derived. Then we derive the energy and enstrophy equations and show that these quantities are conserved in the inviscid limit. The equations and results of this chapter are repeatedly used in the next chapters.

2.1 Navier-Stokes Equations

It is believed that incompressible fluid flow is governed by

$$\partial_t \mathbf{u} + \mathbf{u} \cdot \nabla \mathbf{u} = -\nabla p + \nu \Delta \mathbf{u} + \mathbf{f}, \tag{2.1a}$$

$$\nabla \cdot \mathbf{u} = 0, \tag{2.1b}$$

$$\mathbf{u}(t = 0, \mathbf{x}) = \mathbf{u}_0(\mathbf{x}), \tag{2.1c}$$

where $\mathbf{u}$ is the velocity field, p is the pressure, $\mathbf{f}$ is the external forcing, $\mathbf{u}_0$ is the initial condition and ν is the molecular viscosity. The velocity field, the pressure and the forcing are functions of time (i.e. t) and space(i.e. $\mathbf{x}$). Here we will consider the flow in a two dimensional box with periodic boundary conditions. Therefore $\mathbf{u}$, $\mathbf{f} : \mathbb{R}^+ \times \Omega \to \mathbb{R}^2$ and $p : \mathbb{R}^+ \times \Omega \to \mathbb{R}$ where $\Omega = \mathbb{T}^2$ is the two-dimensional torus. The foricng $\mathbf{f}$ can in general be divergent, however, here it is assumed to be divergence free. We refer to the above partial differential equation as NSE[1].

The Reynolds (Re-) number is defined as $\mathrm{Re} = UL/\nu$ where U is a characteristic velocity and L is a characteristic length scale. One typical choice of characteristic velocity and length scale are respectively the quadratic mean of

[1]Short form for Navier–Stokes equation.

the velocity $\langle|\mathbf{u}|^2\rangle^{1/2}$ and the size of the periodic box $\mathbb{T}^2$. It turns out that the flow becomes more and more "turbulent" as the Re-number increases. Since there is not a unique and generally accepted way of defining the characteristic velocity and length scales, in our numerical simulations we only report the value of the viscosity ν.

The continuity equation (2.1b) implies that the solutions of NSE must be divergence-free. Therefore, we can combine the first two equations into one by projecting the solutions of the momentum equation (2.1a) onto the space of divergence-free vector functions

$$\partial_t \mathbf{u} + \mathbb{P}(\mathbf{u}\cdot\nabla\mathbf{u}) = \nu\Delta\mathbf{u} + \mathbf{f} \tag{2.2}$$

where $\mathbb{P}$ is the projection operator onto the non-divergent vector functions. Note that since the gradient of the pressure is normal to the space of non-divergent vectors, it vanishes after projection.

One can rewrite NSE in terms of the components of the vector quantities as follows

$$\partial_t u_i + u_j\partial_j u_i = -\partial_i p + \frac{1}{\mathrm{Re}}\partial_j\partial_j u_i + f_i, \tag{2.3a}$$

$$\partial_j u_j = 0, \tag{2.3b}$$

where $\partial_j \triangleq \frac{\partial}{\partial x_j}$, $i,j = 1,2$ and Einstein's convention is used for indices, i.e. summation over repeated indices.

Another useful formulation of NSE is the spectral form of he equations in terms of the Fourier transform of the functions.

$$\partial_t\hat{u}_i(\mathbf{k}) + \hat{\imath}k_m(\delta_{ij} - k_ik_j/k^2)\sum_{\mathbf{p}+\mathbf{q}=\mathbf{k}}\hat{u}_j(\mathbf{p})\hat{u}_m(\mathbf{q}) = -\nu k^2\hat{u}_i(\mathbf{k}) + \hat{f}_i(\mathbf{k}) \tag{2.4}$$

where the hat sign refers to Fourier transform except in $\hat{\imath} = \sqrt{-1}$. δ_{ij} is the Kronecker delta function. Note that $\delta_{ij} - k_ik_j/k^2$ is the projection operator $\mathbb{P}$ in Fourier space and that we have used the incompressibility condition $k_j\hat{u}_j = 0$.

The vorticity is defined as $\mathbf{w} = \nabla\times\mathbf{u}$. Note that since we consider the 2-D space, the only nonzero component of the vorticity field is the normal component to the plane of the flow. For simplicity we denote this component by w. In other words, $w = \mathbf{w}\cdot\hat{\mathbf{n}}$ where $\hat{\mathbf{n}}$ is the unit normal vector. One can derive the vorticity equation by taking the curl of equation (2.1a)

$$\partial_t w + \mathbf{u}\cdot\nabla w = \frac{1}{\mathrm{Re}}\Delta w + f_w, \tag{2.5}$$

where $f_w = \partial_1 f_2 - \partial_2 f_1$ is the non-zero component of $\nabla\times\mathbf{f}$. Note that $\nabla\times\nabla p = \mathbf{0}$ and therefore the pressure does not appear in the vorticity equation.

2.1.1 Energy and Enstrophy Equations

We define the instantaneous kinetic energy of the flow at time t by

$$E(t) \triangleq \frac{1}{2}\int_\Omega |\mathbf{u}(t,\mathbf{x})|^2 \,\mathrm{d}\mathbf{x} = \frac{1}{2}(u_i, u_i)_{L^2(\Omega)}, \tag{2.6}$$

where $(\cdot,\cdot)$ is the inner product in the corresponding space. Enstrophy is the energy of the vorticies and is defined by

$$Z(t) \triangleq \frac{1}{2}\int_\Omega |w(t,\mathbf{x})|^2 \,\mathrm{d}\mathbf{x} = \frac{1}{2}(\partial_j u_i, \partial_j u_i)_{L^2(\Omega)}. \tag{2.7}$$

It will be seen shortly that enstrophy determines the rate of energy dissipation.

Using the Fourier transform of the fields one can define the 2-D spectrum of the energy and enstrophy as

$$E(t,\mathbf{k}) \triangleq \frac{1}{2}|\hat{\mathbf{u}}(t,\mathbf{k})|^2, \tag{2.8}$$

and

$$Z(t,\mathbf{k}) \triangleq \frac{1}{2}|\hat{w}(t,\mathbf{k})|^2 = k^2 E(t,\mathbf{k}), \tag{2.9}$$

respectivcly. By averaging over all wave-vectors of the same size one can define the one-dimensional spectra as

$$E(t,k) \triangleq \frac{1}{2}\int_{|\mathbf{k}|=k} |\hat{\mathbf{u}}(t,\mathbf{k})|^2 \,\mathrm{d}S(\mathbf{k}), \tag{2.10}$$

and

$$Z(t,k) \triangleq \frac{1}{2}\int_{|\mathbf{k}|=k} |\hat{w}(t,\mathbf{k})|^2 \,\mathrm{d}S(\mathbf{k}) = k^2 E(t,k), \tag{2.11}$$

where the integration is carried over the circles of radius k.

Note that the total energy $E(t)$, the 2-D energy spectrum $E(t,\mathbf{k})$ and the 1D energy spectrum $E(t,k)$ are all denoted by E. However, we do not expect this to be a source of confusion since the argument of the function clarifies the quantity to which it is referring. Moreover, in the cases where the time dependence of the above functions is trivial we may eliminate t from the arguments.

By multiplying (2.3a) by u_i and integrating over space we will have

$$\frac{d}{dt}E(t) = -2\nu Z(t) + \int_\Omega f_i u_i \,\mathrm{d}\mathbf{x}. \tag{2.12}$$

Note that the non-linear term and the pressure vanish due to incompressibility condition, i.e. $\partial_i u_i = 0$. By integration by parts it follows that

$$\int_\Omega u_i \partial_i p \,\mathrm{d}\mathbf{x} = -\int_\Omega p \partial_i u_i \,\mathrm{d}\mathbf{x} = 0, \tag{2.13}$$

and

$$\int_\Omega u_i u_j \partial_j u_i \, \mathrm{d}\mathbf{x} = \frac{1}{2}\int_\Omega u_j \partial_j (u_i u_i) \, \mathrm{d}\mathbf{x} = -\frac{1}{2}\int_\Omega u_i u_i \partial_j u_j \, \mathrm{d}\mathbf{x} = 0, \tag{2.14}$$

where the boundary terms vanish due to periodic boundary conditions.

Remark: Note that in the absence of external forcing (i.e. $\mathbf{f} \equiv \mathbf{0}$), the energy equation will be $\frac{d}{dt}E(t) = -2\nu Z(t)$. Therefore, as was pointed out earlier, the decay rate of total energy is proportional to the total enstrophy.

Remark: We emphasize that the non-linearity does not appear in the energy equation (2.12) because $(\mathbf{u}\cdot\nabla\mathbf{u}, \mathbf{u})_{L^2(\Omega)^2} = 0$. Therefore, it is an *inertial* term which does not alter the total energy of the system. We will shortly show that this term distributes energy (and enstrophy) among different scales.

A more interesting equation is the one that describes the balance of energy among different modes. One can derive this equation by multiplying (2.4) by $\overline{\hat{u}_i(t,\mathbf{k})}$.

$$\frac{d}{dt}E(t,\mathbf{k}) + T_E(t,\mathbf{k}) = -2\nu k^2 E(t,\mathbf{k}) + F(t,\mathbf{k}), \tag{2.15}$$

where

$$F(t,\mathbf{k}) = \Re\{\hat{f}_i(t,\mathbf{k})\overline{\hat{u}_i(t,\mathbf{k})}\} = \Re\{\hat{\mathbf{f}}(t,\mathbf{k})\cdot\overline{\hat{\mathbf{u}}(t,\mathbf{k})}\}, \tag{2.16}$$

is the energy injected into mode $\mathbf{k}$ by the external forcing. $\Re$ stands for the real part of a complex number. The transfer function $T_E(t,\mathbf{k})$ is defined by

$$\begin{aligned} T_E(t,\mathbf{k}) &= \Re\left\{\hat{\imath}k_m(\delta_{ij} - k_i k_j/k^2)\sum_{\mathbf{p}+\mathbf{q}=\mathbf{k}}\hat{u}_j(t,\mathbf{p})\hat{u}_m(t,\mathbf{q})\overline{\hat{u}_i(t,\mathbf{k})}\right\} \\ &= \Re\left\{\widehat{\mathbb{P}(\mathbf{u}\cdot\nabla\mathbf{u})}\cdot\overline{\hat{\mathbf{u}}(t,\mathbf{k})}\right\}, \end{aligned} \tag{2.17}$$

and represents the energy transferred into (if positive) or out of (if negative) mode $\mathbf{k}$.

A yet more useful equation can be obtained by averaging over all wavevectors of the same amplitude to get

$$\frac{d}{dt}E(t,k) + T_E(t,k) = -2\nu k^2 E(t,k) + F(t,k), \tag{2.18}$$

This equation is in terms of the one-dimensional energy spectrum. It contains less details compared to two-dimensional energy equation, however, it is much easier to work with. The one-dimensional triad function $T_E(t,k)$ is now the total energy transfer to (if positive) or from (if negative) mode k. Therefore, the sum of T_E over all wavenumbers less than a particular wavenumber k shows the flux of energy through that wavenumber. This flux is shown by $\Pi_E(t,k)$ and by definition satisfies

$$\Pi_E(t,k) = \int_0^k T_E(t,\kappa)\,\mathrm{d}\kappa, \tag{2.19}$$

or equivalently

$$\frac{\partial \Pi_E}{\partial k}(t,k) = T_E(t,k). \tag{2.20}$$

Similar evolution equations can be derived for the enstrophy from the vorticity equation (2.5). For instance the one dimensional enstrophy spectrum satisfies

$$\frac{d}{dt}Z(t,k) + T_Z(t,k) = -2\nu k^2 Z(t,k) + k^2 F(t,k), \tag{2.21}$$

where $T_Z(t,k) = k^2 T_E(t,k)$ is the one-dimensional *enstrophy transfer function* and denotes the total enstrophy transfer to (or from) mode k. The enstrophy flux through a wavenumber k is defined as

$$\Pi_Z(t,k) = \int_0^k T_Z(t,\kappa)\,\mathrm{d}\kappa. \tag{2.22}$$

Remark: Since the triad interactions are inertial interactions, the transfer functions preserve the total energy (and enstrophy). In other words,

$$\int_0^\infty T_E(t,k)\,\mathrm{d}k = 0, \tag{2.23}$$

and,

$$\int_0^\infty T_Z(t,k)\,\mathrm{d}k = 0. \tag{2.24}$$

This together with equations (2.18) and (2.21) implies that in the absence of external forcing (i.e. $F(t,k) \equiv 0$) in an inviscid fluid (i.e. $\nu \equiv 0$) the total energy $E(t)$ and the total enstrophy $Z(t)$ are conserved, i.e.

$$\frac{dE(t)}{dt} = 0, \quad \text{and} \quad \frac{dZ(t)}{dt} = 0. \tag{2.25}$$

This simultaneous conservation of energy and enstrophy plays an important role in the formation of dual cascade of energy and enstrophy in 2-D turbulence. Note that the enstrophy conservation is a distinguished feature of 2-D flow and is absent in 3-D. This is a fundamental difference in the dynamics of 2-D and 3-D turbulence.

Remark: To impede a source of mistake, we emphasis that $\Pi_Z(t,k) \neq k^2\Pi_E(t,k)$. The correct identity is $\frac{\partial \Pi_Z}{\partial k}(t,k) = k^2 \frac{\partial \Pi_E}{\partial k}(t,k)$.

2.2 Energy and Enstrophy Triads

As was mentioned before, the non-linear term in NSE plays an important role in the flow dynamics at high Re numbers. Here, the role of this non-linearity in spreading the energy among different scales is demonstrated. For notational

simplicity in this section, T is used instead of T_E and S is used instead of T_Z. Moreover, since the time dependence is clear, the argument t is eliminated from the transfer functions.

The transfer function $T(\mathbf{k})$ has been defined in (2.17). A more detailed quantity is the triad of energy defined as

$$T(\mathbf{k},\mathbf{p},\mathbf{q}) \triangleq \Re\{\hat{i}(\delta_{ij}-k_ik_j/k^2)k_m\hat{u}_j(\mathbf{p})\hat{u}_m(\mathbf{q})\overline{\hat{u}_i(\mathbf{k})}\delta_{\mathbf{k},\mathbf{p}+\mathbf{q}}\}. \tag{2.26}$$

Note that $T(\mathbf{k},\mathbf{p},\mathbf{q}) \neq 0$ if and only if $\mathbf{p}+\mathbf{q}=\mathbf{k}$. Also, the energy triads $T(\mathbf{k},\mathbf{p},\mathbf{q})$ are related to the transfer functions $T(\mathbf{k})$, by

$$T(\mathbf{k}) = \sum_{\mathbf{p},\mathbf{q}} T(\mathbf{k},\mathbf{p},\mathbf{q}). \tag{2.27}$$

The energy triad functions $T(\mathbf{k},\mathbf{p},\mathbf{q})$ represent the instantaneous energy transfer from wave-vectors $\mathbf{p}$ and $\mathbf{q}$ to the wave-vector $\mathbf{k}$.

Similarly, one can define the enstrophy triads $S(\mathbf{k},\mathbf{p},\mathbf{q})$. It is easy to show then that

$$S(\mathbf{k},\mathbf{p},\mathbf{q}) = k^2T(\mathbf{k},\mathbf{p},\mathbf{q}) \tag{2.28}$$

The other property of energy and enstrophy triads is that they satisfy the following conservation equations

$$T(\mathbf{k},\mathbf{p},\mathbf{q}) + T(\mathbf{p},\mathbf{q},\mathbf{k}) + T(\mathbf{q},\mathbf{k},\mathbf{p}) = 0, \tag{2.29a}$$

$$k^2T(\mathbf{k},\mathbf{p},\mathbf{q}) + p^2T(\mathbf{p},\mathbf{q},\mathbf{k}) + q^2T(\mathbf{q},\mathbf{k},\mathbf{p}) = 0, \tag{2.29b}$$

which follow easily from the definition of the triads. Indeed, the above triad conservations are responsible for the conservation of energy and enstrophy which were discussed earlier. Moreover, they provide two equations for three unknowns (i.e energy triads) and therefore non-trivial solutions of the equations exist. In order to calculate these non-trivial solutions, one needs to solve NSE first because by definition the triads depend on the velocity fields. However, we can analyze some properties of these functions without calculating the numerical values. It follows from equations (2.29a) and (2.29b) that

$$\frac{T(\mathbf{k},\mathbf{p},\mathbf{q})}{T(\mathbf{q},\mathbf{k},\mathbf{p})} = \frac{q^2-p^2}{p^2-k^2}, \tag{2.30a}$$

$$\frac{T(\mathbf{p},\mathbf{q},\mathbf{k})}{T(\mathbf{k},\mathbf{p},\mathbf{q})} = \frac{q^2-k^2}{p^2-q^2}, \tag{2.30b}$$

$$\frac{T(\mathbf{q},\mathbf{k},\mathbf{p})}{T(\mathbf{p},\mathbf{q},\mathbf{k})} = \frac{k^2-p^2}{q^2-k^2}. \tag{2.30c}$$

As a result, *the energy is either transferred from intermediate wave-vector to the other two wave-vectors or it is transferred to the intermediate wave-vector*

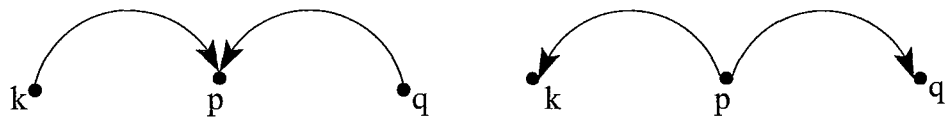

(a) energy/enstrophy transfer *to* the intermediate mode

(b) energy/enstrophy transfer *from* the intermediate mode

Figure 2.1: Possible triad interactions

from the other two wave-vectors (see figure 2.1). The intermediate wave-vector is the one with the intermediate magnitude. As an example, let k=1, p=2 and q=3. Then **p** is the intermediate mode and either

$$T(\mathbf{k},\mathbf{p},\mathbf{q}) < 0,\ T(\mathbf{q},\mathbf{k},\mathbf{p}) < 0,\ T(\mathbf{p},\mathbf{q},\mathbf{k}) > 0, \tag{2.31}$$

or

$$T(\mathbf{k},\mathbf{p},\mathbf{q}) > 0,\ T(\mathbf{q},\mathbf{k},\mathbf{p}) > 0,\ T(\mathbf{p},\mathbf{q},\mathbf{k}) < 0. \tag{2.32}$$

Similar results hold for the enstrophy triads $S(\mathbf{k},\mathbf{p},\mathbf{q})$.

Now assume that among all non-zero triad interactions, the *local* triad interactions are dominant and therefore the *non-local* interactions are negligible. By local triads we mean the triad wave-vectors with "close" magnitude. For such local interactions

$$|T(\mathbf{k},\mathbf{p},\mathbf{q})| > |T(\mathbf{q},\mathbf{k},\mathbf{p})| \tag{2.33a}$$

$$|S(\mathbf{k},\mathbf{p},\mathbf{q})| < |S(\mathbf{q},\mathbf{k},\mathbf{p})| \tag{2.33b}$$

if $k < p < q$. For instance, let $k = n-1$, $p = n$ and $q = n+1$. Note that $\frac{T(\mathbf{k},\mathbf{p},\mathbf{q})}{T(\mathbf{q},\mathbf{k},\mathbf{p})} = \frac{q^2-p^2}{p^2-k^2} = \frac{(n+1)^2-n^2}{n^2-(n-1)^2} > 1$ for all $n \geq 2$ while, $\frac{S(\mathbf{k},\mathbf{p},\mathbf{q})}{S(\mathbf{q},\mathbf{k},\mathbf{p})} = \frac{q^2-p^2}{p^2-k^2} = \frac{(n+1)^2-n^2}{n^2-(n-1)^2} < 1$ as figure 2.2 illustrates.

Inequalities (2.31), (2.32) and (2.33a) suggest that only the following two cases are possible:

i. In the case where energy is transferred from the intermediate mode to the other two modes, most of the energy is transferred to the *smallest* wave-number (figure 2.3a-top).

ii. In the case where energy is transferred to the intermediate mode from the other two modes, most of the energy is provided by the *smallest* wave-number (figure 2.3a-bottom).

On the other hand, inequality (2.33b) suggests that the case for the enstrophy is exactly the opposite:

i. In the case where enstrophy is transferred from the intermediate mode to the other two modes, most of the enstrophy is transferred to the *largest* wave-number (figure 2.3b-top).

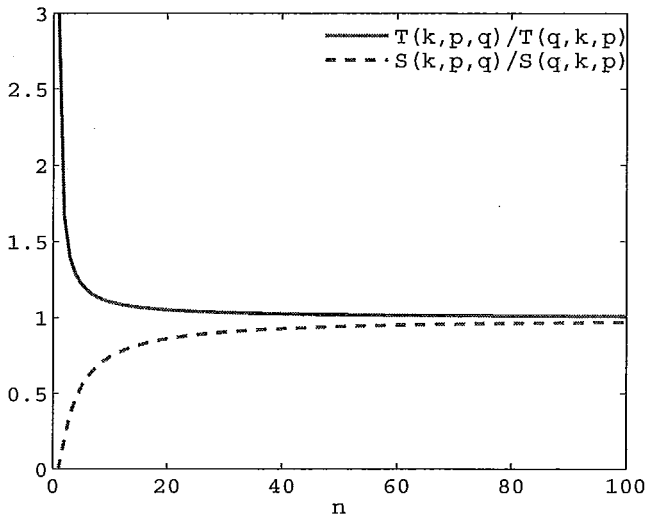

Figure 2.2: The ratio of the energy and enstrophy transfer rates with $k = n - 1$, $p = n$ and $q = n + 1$. The energy is mostly transferred to/from the lower mode while the enstrophy is mostly transferred to/from the higher mode.

ii. In the case where enstrophy is transferred to the intermediate mode from the other two modes, most of the enstrophy is provided by the *largest* wave-number (figure 2.3b-bottom).

In 1953, Fjørtoft [9] showed that most of energy triad interactions are of the first type (i.e. i) while most of enstrophy triad interactions are of the second type (i.e. ii). Therefore, he concluded that in two-dimensional incompressible Navier-Stokes turbulence the energy fluxes *upscale* on average while the enstrophy fluxes *downscale*. Later, numerical simulations of Marilees and Warn [26] confirmed this claim. However, Fjørtoft's argument is based on the assumption that the local triad interactions are dominant. In the next section, we will present a proof of upscale energy and downscale enstrophy fluxes which has been proposed by Gkioulekas and Tung [15] recently and does not assume local triad interactions. Moreover, this proof has interesting consequences which will be helpful in analysis of our numerical results.

2.3 Proof of the Energy and Enstrophy Cascades

In this section, it is shown that in 2-D turbulence energy cascades to larger scales in the net while enstrophy cascades to smaller scales. The proof is due to Gkioulekas and Tung [15]. Here we will briefly sketch the proof and then mention the consecutive results which will be used later. For more details, the reader can refer to [15].

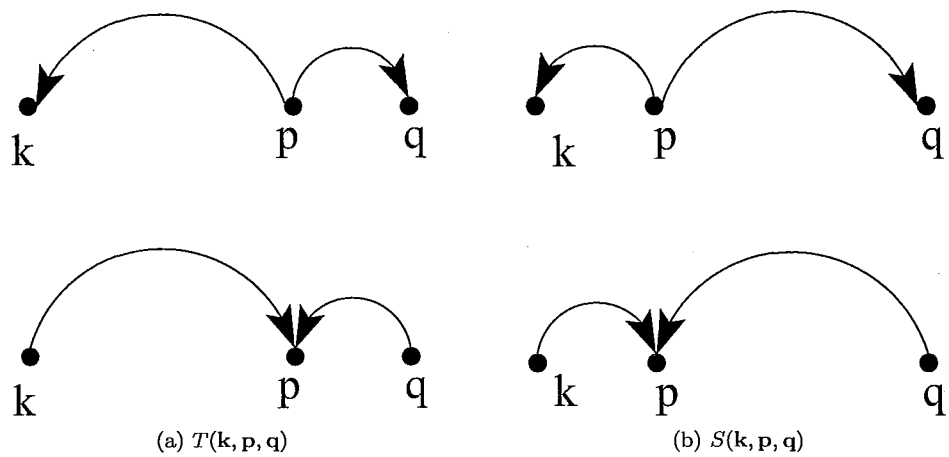

(a) $T(\mathbf{k},\mathbf{p},\mathbf{q})$ (b) $S(\mathbf{k},\mathbf{p},\mathbf{q})$

Figure 2.3: Possible triad interactions

The proof assumes

1. Statistically stationary state
   As a result the energy and enstrophy spectra are stationary, i.e.
   $$\frac{\partial E}{\partial t} \equiv 0 \quad \text{and} \quad \frac{\partial Z}{\partial t} \equiv 0. \tag{2.34}$$
2. Band-limited forcing
   If $F(t,k)$ is the energy injection into mode k by external forcing as defined in section §2.1, then $F(t,k) = 0$ if $k \notin [k_1, k_2]$ where $[k_1, k_2]$ is a narrow band of wavenumbers (see figure 2.4). In other words the forcing is band-limited with the band-width $k_2 - k_1$. It will be shown that this assumption can be replaced by the weaker assumption that at each wavenumber, the energy injection due to the external forcing must be bounded from above by the energy dissipation due to molecular viscosity.

The statistically stationary assumption together with the energy and enstrophy equations (2.18) and (2.21) implies that

$$\frac{\partial \Pi_E(k)}{\partial k} = -2\nu k^2 E(k) + F(k), \tag{2.35a}$$

$$\frac{\partial \Pi_Z(k)}{\partial k} = -2\nu k^2 Z(k) + k^2 F(k). \tag{2.35b}$$

One can integrate these equations over the interval $(0,k)$ with $k < k_1$ to get

$$\Pi_E(k) = -\int_0^k \left(2\nu q^2 E(q) - F(q)\right) \mathrm{d}q \; < 0, \tag{2.36a}$$

$$\Pi_Z(k) = -\int_0^k \left(2\nu q^2 Z(q) - q^2 F(q)\right) \mathrm{d}q \; < 0. \tag{2.36b}$$

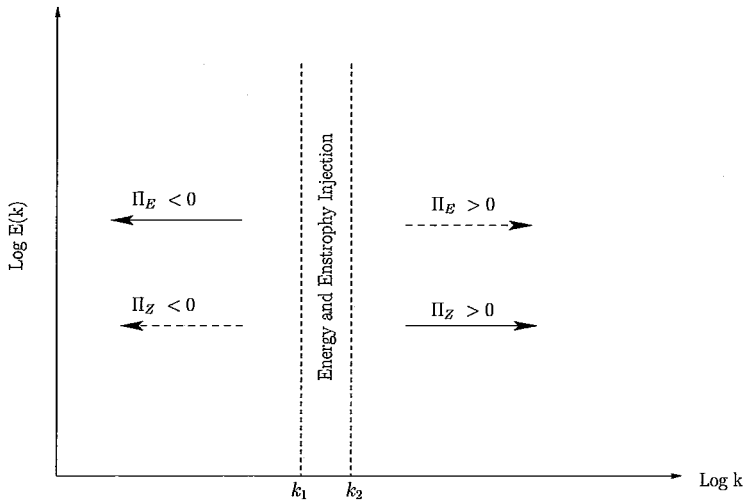

Figure 2.4: The flux of energy and enstrophy in 2D turbulence. The solid arrows refer to the dominant fluxes while the dashed arrows refer to the subordinate fluxes. The energy and enstrophy are injected by the external forcing over the wavenumbers $[k_1, k_2]$

Therefore, for $k < k_1$ the energy and enstrophy fluxes are negative, i.e. the energy and enstrophy *both* cascade to larger scales. Note that $F(t,k) = 0$ for $k < k_1$ and $k > k_2$.

A similar integration on the interval $(k, +\infty)$ with $k > k_2$ leads to

$$\Pi_E(k) = \int_k^\infty \left(2\nu q^2 E(q) - F(q)\right) \, \mathrm{d}q \; > 0, \tag{2.37a}$$

$$\Pi_Z(k) = \int_k^\infty \left(2\nu q^2 Z(q) - q^2 F(q)\right) \, \mathrm{d}q \; > 0. \tag{2.37b}$$

Hence, for $k > k_2$ the energy and enstrophy fluxes are positive, i.e. the energy and enstrophy *both* cascade to smaller scales.

These initial results demonstrate that if energy and enstrophy are injected over a band-width of intermediate wavenumbers, they both cascade to larger scales on the large scale side of the forcing band. At the same time, they both cascade to smaller scales on the small scale side of the injection wavenumbers(see figure 2.4). It may seem paradoxical with the notion of inverse energy and forward enstrophy cascades, however, it should be understood that the inverse and forward cascades refer to average fluxes. As it will be shortly shown the *most* of energy cascades to larger scales while the *most* of enstrophy cascades to smaller scales. Only in the extreme case of infinite Reynolds number (or zero viscosity) *all* of the injected energy (enstrophy) fluxes to the larger (smaller) scales.

Remark: In carrying the above integrations, we have used the fact that $\Pi_E(0) = \Pi_Z(0) = 0$ and $\Pi_E(+\infty) = \Pi_Z(+\infty) = 0$ which follow from the equa-

tions (2.19) and (2.22) together with the conservation conditions $\int_0^\infty T_E(t,k)\,\mathrm{d}k = 0$ and $\int_0^\infty T_Z(t,k)\,\mathrm{d}k = 0$.

The other important inequality which links the energy and enstrophy fluxes reads

$$\Pi_Z(k) - k^2\Pi_E(k) > 0, \tag{2.38}$$

for *any wavenumber* $k \notin [k_1, k_2]$. One can show this, for $k < k_1$, by multiplying the energy flux in equation (2.36) by k^2 and subtracting the result from the enstrophy flux to get

$$\Pi_Z(k) - k^2\Pi_E(k) = \int_0^k (k^2 - q^2)\left(2\nu q^2 E(q) - F(q)\right)\,\mathrm{d}q \; > 0. \tag{2.39}$$

Similarly, it follows from equation (2.37) that

$$\Pi_Z(k) - k^2\Pi_E(k) = \int_k^\infty (q^2 - k^2)\left(2\nu q^2 E(q) - F(q)\right)\,\mathrm{d}q \; > 0, \tag{2.40}$$

for $k > k_2$.

Now we are ready to show that the energy fluxes to larger scales in the net while the enstrophy fluxes to smaller scales. For any $k \notin [k_1, k_2]$ the enstrophy flux satisfies

$$\begin{aligned}\Pi_Z(k) &= \int_0^k \frac{\partial \Pi_Z(q)}{\partial q}\,\mathrm{d}q = \int_0^k q^2 \frac{\partial \Pi_E(q)}{\partial q}\,\mathrm{d}q \\ &= k^2\Pi_E(k) - \int_0^k 2q\Pi_E(q)\,\mathrm{d}q,\end{aligned}$$

therefore,

$$\int_0^k q\Pi_E(q)\,\mathrm{d}q = -\frac{1}{2}\left(\Pi_Z(k) - k^2\Pi_E(k)\right) \; < 0, \tag{2.41}$$

for any $k \notin [k_1, k_2]$. This implies that the the net energy flux is negative and therefore upscale energy flux is dominant. Note that to draw this conclusion it was sufficient to show $\int_0^k \Pi_E(q)\,\mathrm{d}q \; < 0$ which is weaker than $\int_0^k q\Pi_E(q)\,\mathrm{d}q \; < 0$.

On the other hand,

$$\begin{aligned}\Pi_E(k) &= -\int_k^\infty \frac{\partial \Pi_E(q)}{\partial q}\,\mathrm{d}q = -\int_k^\infty q^{-2} \frac{\partial \Pi_Z(q)}{\partial q}\,\mathrm{d}q \\ &= k^{-2}\Pi_Z(k) - \int_k^\infty 2q^{-3}\Pi_Z(q)\,\mathrm{d}q,\end{aligned}$$

and thus

$$\int_k^\infty q^{-3}\Pi_Z(q)\,\mathrm{d}q = \frac{1}{2}k^{-2}\left(\Pi_Z(k) - k^2\Pi_E(k)\right) \; > 0, \tag{2.42}$$

for any $k \notin [k_1, k_2]$. This implies that the the net enstrophy flux is positive and therefore downscale enstrophy flux is dominant. Again, in order to draw

this conclusion it was sufficient to show $\int_k^\infty \Pi_Z(q)\,\mathrm{d}q > 0$ which is weaker than $\int_k^\infty q^{-3}\Pi_Z(q)\,\mathrm{d}q < 0$.

Remark: In [15], it is assumed that the forcing is band limited. However, note that it is not a necessary condition for the dual cascade to exist. If $2\nu k^2 E(t,k) - F(t,k) > 0$, all above calculations still hold and therefore the dual cascade still exist. Therefore, the energy injection does not necessarily need to be zero outside a band of wavenumbers. But it has to be bounded from above by the viscus energy dissipation, i.e. $2\nu k^2 E(t,k)$, at each wavenumber. Therefore, we relax the assumption of band-limited forcing to

$$G(t,k) = 2\nu k^2 E(t,k) - F(t,k) > 0, \quad \forall t,k \in \mathbb{R}^+. \tag{2.43}$$

This condition is used to study the energy and enstrophy transfers in §4.1.

In summary, in a statistically stationary 2-D turbulence, if the energy and enstrophy are injected at a particular wavenumber, they cascade both upscale and downscale due to triad interactions. However, energy cascades upscale mostly while most of the enstrophy cascades downscale. The downscale flux of energy and enstrophy are dissipated eventually at smallest scales by the molecular viscosity. If the flow domain is infinite in both directions, energy and enstrophy keep being transferred to larger and larger scales. However, when the domain is finite (which is the case in lab experiments and numerical simulations), a large scale dissipation mechanism is required to prevent the accumulation of energy and enstrophy at largest available scales. This large scale dissipation and its effect on the dynamics of the flow is described later in more details.

2.4 Power Law scaling of the Energy Spectrum

Here the underlying assumptions of the KLB theory are reviewed and the power law scaling of 2-D turbulence is derived. For more details the reader can refer to [18, 2, 20].

Consider a 2D incompressible flow and assume that energy and enstrophy are injected into the flow by some external forcing over a narrow band of intermediate wavenumbers $[k_1, k_2]$ (see figure 2.4). As was shown in section §2.3, most of the energy then transfers upscale and most of the enstrophy transfers downscale. In a finite domain, the energy dissipates at large scale due to the friction between the box size vortices and the boundary [see 4] while the enstrophy dissipates at small scales due to the molecular viscosity. At large Reynolds numbers (small viscosity), one can neglect the energy/enstrophy dissipation (i.e. $2\nu k^2 E(k)$) unless $\nu k^2 \sim \mathcal{O}(1)$. For instance, if $\nu = 10^{-6}$, dissipation is considerable only at $k > 10^3$ (i.e. at relatively small scales). Let denote the wavenumber at which the small scale dissipation becomes important by k_ν and

neglect the molecular energy dissipation over the range $(0, k_\nu)$. For now suppose that the physical domain is infinite in both directions and therefore there are no large scale energy dissipations. Hence the energy/enstrophy injection and energy/enstrophy dissipation are negligible over $k \in (0, k_\nu) \setminus [k_1, k_2]$. In addition, assume that the upscale enstrophy and downscale energy fluxes are negligible. Then one can assume that there are two inertial ranges upscale and downscale of the injection range $[k_1, k_2]$ since the energy/enstrophy injection and dissipation are negligible and the dynamics of the flow is controlled by the the inertial (i.e. triad) interactions. Let denote the range of wavenumbers over which the energy cascades upscale by $[k_1^e, k_2^e]$ where $0 < k_1^e < k_2^e \leq k_1$. Similarly denote the enstrophy forward cascade by $[k_1^z, k_2^z]$ where $k_2 \leq k_1^z < k_2^z < k_\nu$. For a schematic representation of these ranges refer to figure 2.5.

Also assume that the flow is statistically *homogeneous*. In this case the transfer/injection/dissipation of the energy and enstrophy is almost uniformly distributed in physical space. As a result we can study the Fourier transforms of the energy and enstrophy neglecting the local phenomena in the flow.

Moreover, assume that the flow is statistically *isotropic*, i.e. the statistical quantities do not depend on the direction in which they are measured. As a result the one-dimensional energy spectrum $E(k)$ contains no less information than the two-dimensional spectrum $E(\mathbf{k})$. This simplifies the analysis to a great extent.

In summary, the underlying assumptions of the KLB theory are the following:

1. The flow is statistically steady state.
2. The flow is statistically homogeneous.
3. The flow is statistically isotropic.
4. All of the injected energy fluxes upscale due to inertial interactions over a range of wavenumbers denoted by $[k_1^e, k_2^e]$. Moreover, All of the injected enstrophy fluxes downscale due to inertial interactions over a range of wavenumbers denoted by $[k_1^z, k_2^z]$.
5. Over the energy range $[k_1^e, k_2^e]$, the energy spectrum $E(k)$ depends only on energy injection rate ϵ and wavenumber k. Over the enstrophy inertial range $[k_1^z, k_2^z]$, the energy spectrum depends only on the enstrophy injection rate η and wavenumber.

We are now a dimensional analysis away from the KLB scaling laws. Lets denote the physical dimension of a quantity π by $[\pi]$. Then $[E] = L^3T^{-2}$, $[\epsilon] = L^2T^{-3}$, $[\eta] = T^{-3}$ and $[k] = L^{-1}$ where L is the dimension of length and T is the dimension of time. Also note that the inertial range assumption of

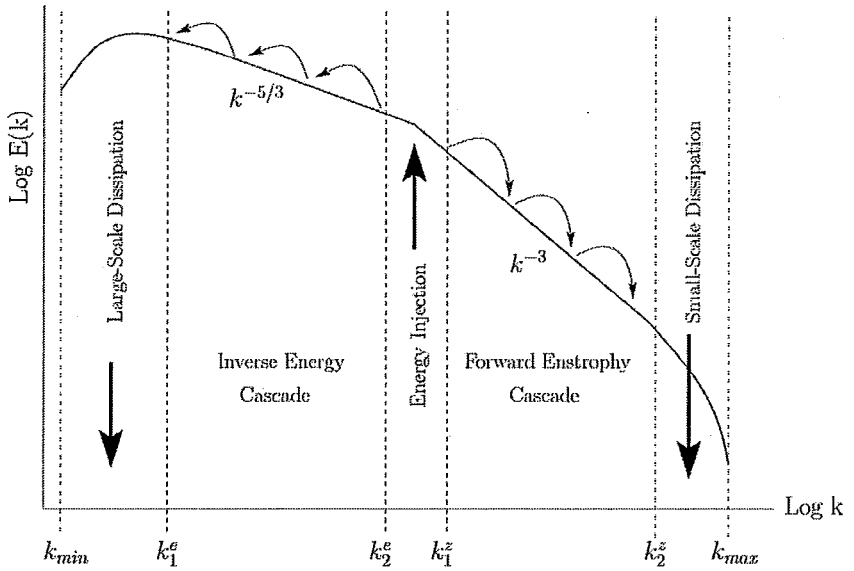

Figure 2.5: Schematic representation of the KLB theory. Energy and enstrophy are injected by the external forcing over the range (k_2^e, k_1^z). Energy and enstrophy inertial ranges are $[k_1^e, k_2^e]$ and $[k_1^z, k_2^z]$ respectively. The smallest wavenumber is $k_{min} = 1$ (if the domain is unbounded $k_{min} = 0$ and the large scale dissipation is not necessary) while the largest available wavenumber k_{max} depends on the numerical resolution. The numerical resolution is usually set such that $k_{max} \approx 2k_\nu$.

the KLB theory implies that over the inverse cascade, energy E is a function of energy injection rate ϵ and wavenumber k while over the forward cascade it is a function of enstrophy injection rate η and wavenumber k. In other words

$$E(k) = f(\epsilon, k), \quad k \in [k_1^e, k_2^e], \tag{2.44a}$$

$$E(k) = g(\eta, k), \quad k \in [k_1^z, k_2^z]. \tag{2.44b}$$

For the physical dimensions to agree the only possible functions f and g are $C\epsilon^{2/3}k^{-5/3}$ and $C'\eta^{2/3}k^{-3}$ respectively where C and C' are dimensionless constants. Therefore, one expects based on this argument that the energy scales as

$$E(k) = \begin{cases} C\epsilon^{2/3}k^{-5/3} & k_1^e \le k \le k_2^e \\ C'\eta^{2/3}k^{-3} & k_1^z \le k \le k_2^z \end{cases} \tag{2.45}$$

This power law is referred to as the KLB scaling law and was first proposed by Kraichnan [18] in 1967. This power law scaling and the various parts of the energy spectrum are illustrated in figure 2.5.

A few remarks are in order.

Remark: Later Kraichnan [19] introduced a logarithmic correction in the scaling laws which is necessary due to the presence of coherent vortices. However, as long as this work is concerned this correction can be neglected. Therefore, we consider the original scalings introduced above.

Remark Note that KLB theory neglects the inverse enstrophy and forward energy cascades. However, in reality there are small fractions of upscale enstrophy flux and downscale energy flux.

Remark: At this point it is necessary to emphasize that KLB theory does not make any comments on the energy/enstrophy injection mechanism, i.e. forcing, except that it is band-limited (or monoscale). Because of the statistically steady state assumption, it is clear that the energy and enstrophy injections must be at a reasonable rate such that after a sufficient elapse of time they balance with the large and small scale dissipations. It is assumed that the space-time structure of the forcing does not have determining effects as long as the scaling laws are concerned. Therefore, in numerical simulations the forcing is (almost) always white noise in time and random in phase. However, our results show, in contrast to what is usually assumed, that the detailed space-time structure of the forcing has a significant effect on the dynamics of the flow and in particular the scaling of the energy spectrum. For details refer to §4.2.

2.5 External Forcing as an Energy and Enstrophy Injection Mechanism

As was mentioned, in 2-D turbulence, energy and enstrophy are distributed among scales through the triad interactions. These interactions are inertial in the sense that they preserve the total energy and only transfer it from one scale to another. The KLB theory provides an statistical description on the energy budget of each scale in a statistically stationary state. This theory is based on the assumption that if the forcing is limited to a narrow band of wavenumbers and the viscosity is small enough (ideally zero) then the dynamics in most of the scales is exclusively due to triad interactions. Since the scales of energy/enstrophy injection are distinct from inertial scales, it is natural to assume that the type of forcing does not affect the scaling over inertial ranges. Therefore, in (most) numerical simulations a simple model of a stirring force which has a constant magnitude in time with random phase in space is employed. In the case that the boundary conditions are periodic, one can define such a forcing by its Fourier transform as

$$\hat{\mathbf{f}}(t,\mathbf{k}) = \frac{\langle -k_y, k_x\rangle}{k^2} A e^{2\pi i \hat{\xi}(t,\mathbf{k})} \chi_{(k_2^e,k_1^z)}(\mathbf{k}) \tag{2.46}$$

where $\mathbf{k} = \langle k_x, k_y\rangle$, $k = |\mathbf{k}|$, A is a constant equal to the magnitude of the forcing and $0 \leq \xi \leq 1$ is a random variable in time and wavevector in the sense that for each t and $\mathbf{k}$, it is randomly chosen between 0 and 1. The characteristic function χ is 1 if $k \in (k_2^e, k_1^z)$ and 0 otherwise. The multiple $\langle -k_y, k_x\rangle/k^2$ is

introduced in order to enforce the divergence free condition $\nabla \cdot \mathbf{f} = 0$.

Such stirring forcings were first suggested for 3-D isotropic turbulence by Martin and Dominicis [25] and Yakhot [42]. The phase structure of this forcing being random is favorable for producing isotropic turbulence. Moreover, the spatial correlation of it can be controlled by the characteristic function χ. To state this more rigorously, define the correlation function of a vector field $\mathbf{u}$ by

$$R_{\mathbf{u}}(\tau, \mathbf{r}) = \langle \mathbf{u}(t, \mathbf{x}) \cdot \mathbf{u}(t + \tau, \mathbf{x} + \mathbf{r}) \rangle \tag{2.47}$$

where $\langle\ \rangle$ denotes time average in time and space. Then the correlation function of the forcing in (2.46) reads

$$R_{\mathbf{f}}(\tau, \mathbf{r}) = \delta(\tau)\chi_{(r_1,r2)}(|\mathbf{r}|) \tag{2.48}$$

where δ is the Kronecker delta and (r_1, r_2) is the range of scales over which the forcing is non-zero with $r_1 \propto 1/k_1^z$ and $r_2 \propto 1/k_2^e$. The forcings in most numerical simulations [see, e.g., 21, 3] which study the isotropic two dimensional turbulence share the essential properties of the above forcing with slightly different formulations.

When the flow domain is finite (which is the case in all numerical simulations) some controversies arise. Constantin et al. [7] proved that the band-limited forcing is inconsistent with the KLB theory in the sense that the slope of the energy spectrum on the enstrophy cascade range will be much steeper than the KLB prediction, i.e. -3. Later, Tran and Shepherd [36] obtained the same result through a different approach. They show that a large-scale sink of energy is necessary for the KLB theory to be observed in finite domains. We discuss this inconsistency rather qualitatively here and will summarize some of the results. For more details the reader can refer to the above-mentioned articles.

Since in 2-D turbulence energy cascades to larger scales, it is natural to expect that the energy will pile up at largest scales when the domain size is finite. This was predicted by Kraichnan himself from the very beginning [18]. As a result some large scale vortices will form after sufficient time. These vortices dominate the flow and do not provide enough space for the enstrophy to cascade to small scales. Therefore, most of the enstrophy will dissipate at scales close to the forcing scale. This results in a steep energy spectrum over the enstrophy cascade range. It is shown in [36] that the slope of the energy spectrum in this case must be steeper than -5 which contradicts with the prediction of the KLB theory, i.e. -3.

It is shown in [36] that if the energy is removed from large scales in order to avoid accumulation of energy, then the KLB scalings may be retrieved. One way (and probably the most straight forward way) to create this large scale

sink of energy is to add the so-called "inverse viscosity"[2] to the Navier–Stokes equation (2.1a). Mathematically speaking, the inverse viscosity of order p_i is obtained by applying the inverse Laplacian operator to the velocity field, i.e.

$$D\mathbf{u} \triangleq \nu_i(-\Delta)^{-p_i}\mathbf{u} \tag{2.49}$$

with $p_i = 0, 1, 2, \cdots$. The constant ν_i determines the intensity of the dissipation. The index i refers to *infrared* (large-scale). Note that the inverse viscosity dissipates energy at a rate of $2\nu_i k^{-2p_i}E(t,k)$ where the energy spectrum $E(t,k)$ is defined in (2.10). Therefore, the energy dissipation due to inverse viscosity is significant at large scales (small k) and negligible for small scales (large k). When $p_i = 0$ the dissipation mechanism is called *Ekman friction* or *linear drag*. Ekman friction is similar to the friction of the atmospheric flow with the earth surface [4]. However, higher orders of inverse viscosity (i.e. $p_i \geq 1$) do not have a physical relevance.

In the presence of inverse viscosity, NSE becomes

$$\partial_t\mathbf{u} + \mathbf{u}\cdot\nabla\mathbf{u} = -\nabla p + \nu\Delta\mathbf{u} - \nu_i(-\Delta)^{-p_i}\mathbf{u} + \mathbf{f}, \tag{2.50a}$$

$$\nabla\cdot\mathbf{u} = \mathbf{0}, \tag{2.50b}$$

$$\mathbf{u}(t=0,\mathbf{x}) = \mathbf{u}_0(\mathbf{x}). \tag{2.50c}$$

Note that the energy injection by forcing and large-scale energy dissipation are given by $F(t,k)$ and $2\nu_i k^{-2p_i}E(t,k)$ respectively where energy injection $F(t,k)$ is calculated by (2.16). Similarly, enstrophy injection by forcing and small-scale enstrophy dissipation are given by $k^2F(t,k)$ and $2\nu k^4E(t,k)$ respectively. In order to reach the statistically stationary state (required for the KLB theory) the energy/enstrophy injection must balance with energy/enstrophy dissipation. In numerical simulations, one can balance them by adjusting the forcing magnitude A in (2.46) and the coefficients of viscosity ν and ν_i.

The above short description speaks volume to the profound effect of the energy/enstrophy injection and dissipation mechanisms on the dynamics of the 2-D turbulent flow and in particular on its scaling of the energy spectrum. On the other hand, however, the forcing and large-scale dissipation used in numerical simulations are chosen to be conveniently implemented in a computational setting. It is assumed that detailed properties of the forcing (such as its phase structure) do not alter the inertial range dynamics of the flow. However, one of the main results that we present in chapter 4 shows the contrary: a particular choice of forcing and large-scale dissipation *can* significantly alter the scaling of the energy spectrum of the flow.

[2] In some texts inverse viscosity is referred to as *hypoviscosity*.

Chapter 3

Numerical Method

3.1 Optimal Control Method

As was mentioned previously, there is not a well justified criterion for the forcing function in 2D turbulence. In numerical simulations, it has become a tradition to use a particular forcing (such as random-phase white noise) and then calculate the resulting energy spectrum. Here we introduce an opposite approach in the sense that we consider a *target* energy spectrum and then find a forcing which will result in that particular forcing. The target energy spectrum in the present study (almost always) follows the KLB scaling laws, i.e. $E \sim k^{-5/3}$ over the large scale side of the spectrum and $E \sim k^{-3}$ over the small scale side (see figure 2.5). Because of the complex structure of the Navier–Stokes equations, finding the corresponding forcing for a particular target energy spectrum is by no means a trivial task. However, using the techniques from optimal control theory it is possible to find a numerical answer for such problems.

Here, the general ideas are described. They will shortly be formulated in a mathematically rigrous way. For any possible energy spectrum, it is required to define its *difference* from the target spectrum (in this case KLB spectrum) in an appropriate way. Then the problem boils down to minimizing the difference between the energy spectrum which is obtained from solving NSE with some particular forcing and the target spectrum. One can start from an arbitrary forcing and then calculate the difference between the resulting spectrum and the target spectrum. The next choice of the forcing should be one that results in a smaller difference between the spectra. The criterion for updating the forcing comes from an idea in multivariable calculus. Note that a mutivariable function decreases in the opposite direction of its gradient. If this gradient direction is somehow known, then the forcing can be updated by moving from the previous forcing in the opposite direction of that gradient by some *appropriate* increment. Continuing the same procedure from the

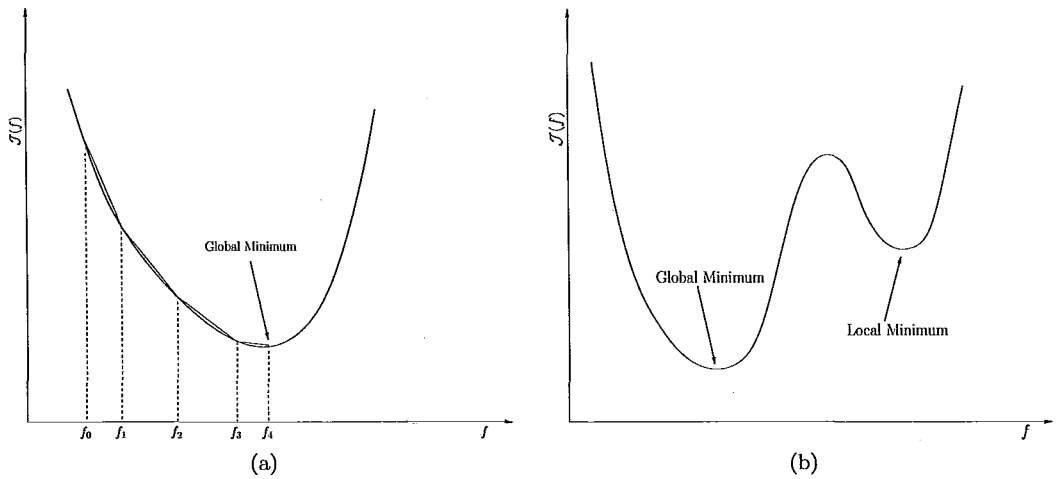

Figure 3.1: Schematic representation of a convex (a) and a non-convex (b) optimization problems. When the problem is convex, by starting from some initial guess f_0 and following the descend direction one will finally find the global minimum. While in a non-convex problem which has more than one local minimizer, depending on the initial guess, one may or may not find the global minimum.

new forcing a closer spectrum to the target will be found. After sufficient iterations, the difference between the spectra will be minimized. If we are lucky enough this minimum is zero and the calculated spectrum coincides with the target spectra. If the problem has a unique local/global minimizer or in other words if it is convex, then we can get close to the global minimum after sufficient iterations. However, if the problem is not convex then there are no guarantee to reach the global minimum. Depending on the starting point (i.e. initial guess) we may get trapped in some local minimizer and never reach the global minimum. The difference between a convex and a non-convex problem is illustrated schematically in figure 3.1 for a single variable function. In a multivariable or an infinite dimensional problem the situation is much more complicated.

Before formulating the optimization problem, we recall some fundamental definitions and theorems of functional analysis.

Definition 3.1.1 (Dual Space). *Consider a Banach space X. A map $\mathcal{J} : X \to \mathbb{R}$ is called a* functional *on X. The set of all continuous linear functionals on X is called the* dual space *of X and is denoted by X^*.*

Definition 3.1.2 (Gâteaux Derivative). *Consider a Banach space X and let $f, f' \in X$. The* Gâteaux differential *of a functional $\mathcal{J} \in X^*$ at f in direction f' is defined as*

$$\mathcal{J}'(f; f') \triangleq \lim_{\epsilon \to 0} \frac{\mathcal{J}(f + \epsilon f') - \mathcal{J}(f)}{\epsilon}, \tag{3.1}$$

if the limit exists. If the limit exists for all $f' \in X$ then $\mathcal{J}$ is Gâteaux differentiable *at f.*

Note that Gâteaux differential is a generalized definition for the directional derivative in multivariable calculus. This general definition is necessary when the space over which the function/functional is defined is infinite dimensional or it does not posses a Hilbert structure. We deal with the former case in our study. Also note that for a fixed $f \in X$ the Gâteaux differential is a functional on X and therefore $\mathcal{J}' \in X^*$. In some texts the differential of $\mathcal{J}$ at f is shown by $D\mathcal{J}_f$.

The following theorem allows us to represent some functionals with an inner product if the space on which the functional is defined possesses a Hilbert structure.

Theorem 3.1.1 (Riesz Representation Theorem). *Consider a Hilbert space X with the inner product $(\cdot,\cdot)_X$. Let $\mathcal{J}$ be a continuous linear functional on X, i.e. $\mathcal{J} \in X^*$. Then there is a unique element $u^* \in X$ such that*

$$\mathcal{J}(f) = (f, u^*)_X, \tag{3.2}$$

for all $f \in X$.

Note the constraints of the theorem: First, the space must be a Hilbert space, i.e. an inner product must be defined on the space. Secondly, the functional must be continuous and linear. Hereafter, Riesz representation theorem will be abbreviated by RRT.

Now consider the incompressible Navier–Stokes equations on a two-dimensional box (Ω) with doubly periodic boundary conditions, i.e. Ω is the two-dimensional torus $\mathbb{T}^2$.

$$\mathcal{L}(\mathbf{u}) \triangleq \partial_t \mathbf{u} + \mathbf{u}\cdot\nabla\mathbf{u} + \nabla p - \nu\Delta\mathbf{u} = \mathbf{f}, \tag{3.3a}$$

$$\nabla\cdot\mathbf{u} = 0, \tag{3.3b}$$

$$\mathbf{u}(t=0,\mathbf{x}) = \mathbf{u_0}(\mathbf{x}), \tag{3.3c}$$

where $\mathbf{u}(t,\cdot) : \Omega \to \mathbb{R}^2$ is the velocity field, $p(t,\cdot) : \Omega \to \mathbb{R}$ is the pressure, ν is the coefficient of kinematic viscosity and $\mathbf{f}(t,\cdot) : \Omega \to \mathbb{R}^2$ is the external forcing. For any solution of NSE we define the one-dimensional energy spectrum as

$$E(t,k) = \frac{1}{2}\int_{\mathcal{C}(k)} |\hat{\mathbf{u}}(t,\mathbf{k})|^2 \, \mathrm{d}S(\mathbf{k}), \tag{3.4}$$

where $\hat{\mathbf{u}}$ is the Fourier transform of $\mathbf{u}$ and $\mathbf{k}$ is the wave vector. $\mathcal{C}(k)$ is a circle with diameter k in 2-D plane, $\mathcal{C}(k) = \{\mathbf{k} \in \mathbb{R}^2 : |\mathbf{k}| = k\}$.

Let $E_0(k)$ be the energy spectrum predicted by KLB theory, i.e.,

$$E_0(k) = \begin{cases} C_1 k^{-5/3} & k_1^e \le k \le k_2^e \\ C_2 k^{-3} & k_1^z \le k \le k_2^z \end{cases}, \tag{3.5}$$

where $[k_1^e\,,\,k_2^e]$ and $[k_1^z\,,\,k_2^z]$ are the energy and enstrophy inertial ranges respectively (figure 2.5). For notational simplicity we denote the union of the inertial ranges by I, i.e. $I = [k_1^e\,,\,k_2^e] \cup [k_1^z\,,\,k_2^z]$. The wavenumber k_1^e may extend to the smallest wavenumbers, k_2^z extends up to the beginning of the dissipation range and $k_2^e < k_1^z$. In the case of monoscale forcing, k_2^e and k_1^z are almost equal to the forcing wavenumber. In the case of band-limited forcing the energy/enstrophy injection range is (k_2^e, k_1^z) or a subset of it. C_1 depends only on the energy dissipation rate (ϵ) and C_2 depends only on the enstrophy dissipation rate (η). Since the energy and enstrophy dissipation rates are constants (based on KLB theory), C_1 and C_2 are also constants. Using the inertial range hypothesis, dimensional analysis gives $C_1 \propto \epsilon^{2/3}$ and $C_2 \propto \eta^{2/3}$. The constants of proportionality are non-dimensional and of order of unity [7]. The target energy spectrum is a slightly different formulation of the KLB spectrum in Eq. (3.5).

The goal is to find a forcing, $\mathbf{f}$, which results in a solution of Navier–Stokes equation (3.3) with the KLB energy spectrum $E_0(k)$. Define the following cost functional:

$$\mathcal{J}(\mathbf{f}) \triangleq \frac{1}{2}\int_0^T \int_I w(t,k)|E(t,k) - E_0(k)|^2 \,\mathrm{d}k\,\mathrm{d}t. \tag{3.6}$$

This functional measures the total difference between the target energy spectrum E_0 and the calculated spectrum E over all wavenumbers in the cascade range and over time. The function $w(t,k)$ is a positive weight function which normalizes $|E(t,k) - E_0(k)|^2$ over the inertial ranges. Since $E_0(k)$ decreases as k^{-3} on the interval $[k_1^z\,,\,k_2^z]$, $w(t,k) = k^6\,\alpha(t)$ is a suitable candidate. The time dependence of the weight function $\alpha(t)$ is used to put more emphasis on the contribution of $E(t,k)$ near $t = T$. This allows the energy spectrum of the flow to evolve gradually from the initial energy spectrum $E(0,k)$ (which is arbitrary due to universality of the KLB theory) toward its equilibrium $E_0(k)$. For example, $\alpha(t)$ can be an strictly increasing linear function (i.e. $\alpha(t) = t/T$) or a step function which is 0 on some interval $[0\,,\,T_1)$ and 1 on $[T_1\,,\,T]$. If for some solution of equation (3.3), the above cost functional is zero, the energy spectrum will scale as predicted by KLB theory on the time interval $[0\,,\,T]$. In this case, the energy spectrum will be stationary for times when $w(t,k) > 0$. However, note that this does not imply, by itself, the existence of the dual cascades with the constant energy and enstrophy fluxes. The dynamics of the cascades must be examined independently. We will get back to this later.

The above description may be formulated as the following optimization problem.

$$\min_{\mathbf{f}\in\mathcal{U}} \mathcal{J}(\mathbf{f}), \tag{3.7}$$

where $\mathcal{U}$ is a suitable function space with Hilbert structure. Here we con-

sider the space of square integrable functions in space and time i.e., $\mathcal{U} = L^2([0,T];L^2(\Omega))$, with the inner product

$$(\mathbf{f},\mathbf{g})_{\mathcal{U}} = \int_0^T \int_\Omega \mathbf{f}(t,\mathbf{x})\cdot\mathbf{g}(t,\mathbf{x})\ \mathrm{d}\mathbf{x}\ \mathrm{d}t, \tag{3.8}$$

for $\mathbf{f},\mathbf{g}\in\mathcal{U}$. Therefore, only the forcings are considered as a valid solution that satisfy

$$\int_0^T \int_\Omega |\mathbf{f}(t,\mathbf{x})|^2\ \mathrm{d}\mathbf{x}\ \mathrm{d}t < \infty, \tag{3.9}$$

which loosly speaking means that the forcing is bounded in amplitude. One can consider smoother forcings by making a different choice of the control space. The cost functional $\mathcal{J}$ depends on $\mathbf{f}$ through the system of equations (3.3) in which the explicit dependence of cost functional on the velocity field has been dropped. This type of cost functional is called a *reduced* cost functional.

Now, the goal is to find a forcing $\mathbf{f}_{\text{opt}}\in\mathcal{U}$ that minimizes the cost functional $\mathcal{J}$. Starting with an initial guess $\mathbf{f}^{(0)}$, an approximation of the minimizer can be found using a gradient-based descent method of the form

$$\mathbf{f}^{(n+1)} = \mathbf{f}^{(n)} + \tau^{(n)}\,\mathcal{A}\nabla\mathcal{J}(\mathbf{f}^{(n)})\ ,\quad n=0,1,\dots, \tag{3.10}$$

such that $\lim_{n\to\infty}\mathbf{f}^{(n)} = \mathbf{f}_{\text{opt}}$ where n is the iteration count and $\tau\in\mathbb{R}^-$ is a constant to be determined at each iteration. At each iteration, the descent direction $\mathcal{A}\nabla\mathcal{J}$ is calculated based on the gradient of the cost functional $\nabla\mathcal{J}$. Different forms of the operator $\mathcal{A}$ correspond to different variants of the gradient method. For instance, if $\mathcal{A}$ is the identity operator, it corresponds to the steepest descent method and if it is an appropriate affine operator, it corresponds to the conjugate gradient method. Since $\tau<0$, the former (i.e. steepest descend) corresponds to moving in the oposite direction of the gradient. Refer to [27] for further details on the steepest descend and conjugate gradient methods As will be shown below, the gradient $\nabla\mathcal{J}$ may be expressed in terms of the solution of a suitably-defined adjoint system.

The necessary condition characterizing the minimizer $\mathbf{f}_{\text{opt}}$ of the cost functional is the vanishing of the Gâteaux differential $\mathcal{J}':\mathcal{U}\times\mathcal{U}\to\mathbb{R}$, i.e.,

$$\mathcal{J}'(\mathbf{f}_{\text{opt}};\mathbf{f}') = 0\ ,\quad \forall\,\mathbf{f}'\in\mathcal{U}, \tag{3.11}$$

where the Gâteaux differential is defined in (3.1). Substituting from (3.4) and (3.6) into (3.1), one can easily show that

$$\mathcal{J}'(\mathbf{f};\mathbf{f}') = \frac{1}{2}\int_0^T\int_I w(t,k)(E(t,k)-E_0(k))\left(\int_{\mathcal{C}(k)}(\widehat{\mathbf{u}}\cdot\overline{\widehat{\mathbf{u}'}}+\overline{\widehat{\mathbf{u}}}\cdot\widehat{\mathbf{u}'})\ \mathrm{d}S(\mathbf{k})\right)\ \mathrm{d}k\ \mathrm{d}t, \tag{3.12}$$

where the bar represents the complex conjugate and $\widehat{\mathbf{u}'}$ is the Fourier transform of the solutions of the Navier–Stokes equations linearized around the state $\mathbf{u}$, i.e,

$$\mathcal{L}'\mathbf{u}' \triangleq \partial_t \mathbf{u}' + \mathbf{u}' \cdot \nabla \mathbf{u} + \mathbf{u} \cdot \nabla \mathbf{u}' + \nabla p' - \nu \Delta \mathbf{u}' = \mathbf{f}', \tag{3.13a}$$

$$\nabla \cdot \mathbf{u}' = 0, \tag{3.13b}$$

$$\mathbf{u}'(t = 0, \mathbf{x}) = 0, \tag{3.13c}$$

where $\mathbf{f}'$ is the *direction* in which the Gâteaux differential is computed in (3.1).

On the other hand, RRT guarantees existence of a unique corresponding element $\nabla \mathcal{J} \in \mathcal{U}$ which satisfies the Riesz identity

$$\mathcal{J}'(\mathbf{f}; \mathbf{f}') = (\nabla \mathcal{J}, \mathbf{f}')_{\mathcal{U}} \ , \ \forall \mathbf{f}' \in \mathcal{U}, \tag{3.14}$$

where $(\cdot, \cdot)_{\mathcal{U}}$ is the L^2-inner product. Hereafter, the subscript $\mathcal{U}$ is eliminated from the inner product. Here we consider only the L^2-functions, however, the approach can be easily generalized to different Hilbert spaces and, in particular, Sobolev spaces [29]. Note that $\nabla \mathcal{J}$ is the steepest ascent direction for the cost functional $\mathcal{J}$. An experesion for the gradient $\nabla \mathcal{J}$ cannot be derived imediately by equating (3.12) and (3.14) since in (3.12) the direction $\mathbf{f}'$ is hidden in $\mathbf{u}'$. However, the following duality pairing argument suggests a governing equation for the gradient.

For any $\mathbf{u}^* \in \mathcal{U}$, $(\mathbf{u}^*, \mathbf{f}') = (\mathbf{u}^*, \mathcal{L}'\mathbf{u}')$ by (3.13). On the other hand,

$$(\mathbf{u}^*, \mathcal{L}'\mathbf{u}') = (\mathcal{L}^*\mathbf{u}^*, \mathbf{u}'), \tag{3.15}$$

where the adjoint operator $\mathcal{L}^*$ reads

$$\mathcal{L}^*\mathbf{u}^* = -\partial_t \mathbf{u}^* - \left[\nabla \mathbf{u}^* + \nabla \mathbf{u}^{*^T}\right] \mathbf{u} - \nabla p^* - \nu \Delta \mathbf{u}^*, \tag{3.16}$$

and can be obtained by integration by parts. Note that the boundary terms resulting from integration by parts in space cancel out due to the periodic boundary conditions. Assuming $\mathbf{u}^*(t = T, \mathbf{x}) = 0$, the terms $\int_{\mathbb{T}} \mathbf{u}^* \cdot \mathbf{u}'|_{t=T} \ \mathrm{d}\mathbf{x}$ and $\int_{\mathbb{T}} \mathbf{u}^* \cdot \mathbf{u}'|_{t=0} \ \mathrm{d}\mathbf{x}$, resulting from integration by parts in time, also vanish since $\mathbf{u}'(t = 0, \mathbf{x}) = 0$.

By Parseval identity,

$$\begin{aligned}(\mathcal{L}^*\mathbf{u}^*, \mathbf{u}') &= \left(\widehat{\mathcal{L}^*\mathbf{u}^*}, \widehat{\mathbf{u}'}\right) \\ &= \int_0^T \int_0^\infty \left(\int_{\mathcal{C}(k)} \widehat{\mathcal{L}^*\mathbf{u}^*} \cdot \overline{\widehat{\mathbf{u}'}} \ \mathrm{d}S(\mathbf{k}) \right) \ \mathrm{d}k \ \mathrm{d}t,\end{aligned} \tag{3.17}$$

where the hat signs represent the Fourier transform. Since $(\mathcal{L}^*\mathbf{u}^*, \mathbf{u}')$ is real valued $(\mathcal{L}^*\mathbf{u}^*, \mathbf{u}') = \frac{1}{2}\left((\widehat{\mathcal{L}^*\mathbf{u}^*}, \widehat{\mathbf{u}'}) + \overline{(\widehat{\mathcal{L}^*\mathbf{u}^*}, \widehat{\mathbf{u}'})}\right)$. Therefore,

$$(\mathcal{L}^*\mathbf{u}^*, \mathbf{u}') = \frac{1}{2} \int_0^T \int_0^\infty \left(\int_{\mathcal{C}(k)} (\widehat{\mathcal{L}^*\mathbf{u}^*} \cdot \overline{\widehat{\mathbf{u}'}} + \overline{\widehat{\mathcal{L}^*\mathbf{u}^*}} \cdot \widehat{\mathbf{u}'}) \ \mathrm{d}S(\mathbf{k}) \right) \ \mathrm{d}k \ \mathrm{d}t. \tag{3.18}$$

A Comparison between (3.12) and (3.18) suggests that if

$$\widehat{\mathcal{L}^*(\mathbf{u}^*)}(t,\mathbf{k}) = w(t,k)(E(t,k) - E_0(k))\hat{\mathbf{u}}(t,\mathbf{k}), \tag{3.19}$$

then $(\mathcal{L}^*\mathbf{u}^*, \mathbf{u}') = \mathcal{J}'(\mathbf{f};\mathbf{f}')$. Since $(\mathbf{u}^*, \mathbf{f}') = (\mathcal{L}^*\mathbf{u}^*, \mathbf{u}')$, it follows from Riesz identity (3.14) that $\nabla\mathcal{J} = \mathbf{u}^*$. Therefore, the gradient direction coincides with the solution of the *adjoint* system

$$\left(\partial_t\mathbf{u}^* + \left[\nabla\mathbf{u}^* + \nabla\mathbf{u}^{*^T}\right]\mathbf{u} + \nabla p^* + \nu\Delta\mathbf{u}^*\right)^\wedge(t,\mathbf{k}) = -w(t,k)(E(t,k)-E_0(k))\hat{\mathbf{u}}(t,\mathbf{k}), \tag{3.20a}$$

$$\nabla\cdot\mathbf{u}^* = 0, \tag{3.20b}$$

$$\mathbf{u}^*(t=T,\mathbf{x}) = 0. \tag{3.20c}$$

By solving the adjoint system to compute the gradient $\nabla\mathcal{J}$ and using the iterative process (3.10), one can find an approximation of the minimizer, $\mathbf{f}_{\text{opt}}$. The optimal value for the parameter τ in (3.10) is the one that minimizes the single variable function $\mathcal{G}(\tau) := \mathcal{J}\left(\mathbf{f}^{(n)} + \tau\,\mathcal{A}\nabla\mathcal{J}(\mathbf{f}^{(n)})\right)$ for fixed $\mathbf{f}^{(n)}$ and $\mathcal{A}\nabla\mathcal{J}(\mathbf{f}^{(n)})$. Here, a standard line minimization method [27] is used to find the appropriate value of τ at each iteration.

In practise, those forcings with very large amplitudes are not of interest. To exclude such forcings, a penalty term is added to the cost functional as follows

$$\mathcal{J}_\eta(\mathbf{f}) = \mathcal{J}(\mathbf{f}) + \frac{1}{2}\eta\,\|\mathbf{f}\|^2, \tag{3.21}$$

where $\mathcal{J}(\mathbf{f})$ is the same as in (3.6), $\eta \in \mathbb{R}^+$ is a constant and $\|\cdot\|$ is the norm in $\mathcal{U}$ (L^2-norm here). The constraint on the norm of the control variable $\mathbf{f}$ is determined by the parameter η. Smaller values of η allow forcings with larger norms and vice versa. Since the Gâteaux differential of the penalty term $\frac{1}{2}\eta\,\|\mathbf{f}\|^2$ in direction $\mathbf{f}'$ is $\eta\,(\mathbf{f},\mathbf{f}')_\mathcal{U}$, the gradient of the modified cost functional is $\nabla\mathcal{J}_\eta(\mathbf{f}) = \mathbf{u}^* + \eta\,\mathbf{f}$ where $\mathbf{u}^*$ is the solution of the previous adjoint system (3.20).

To summarize, the optimization process can be expressed in the following algorithm.

Algorithm 3.1.1.

1. Choose an initial guess $\mathbf{f}^{(0)}(t,\mathbf{x})$; $n = 0$.
2. Solve Navier–Stokes equation (3.3) forward in time with $\mathbf{f} = \mathbf{f}^{(n)}$.
3. Solve adjoint equation (3.20) backward in time.
4. Obtain the cost functional gradient as $\nabla\mathcal{J}_\eta = u^* + \eta\mathbf{f}$
5. Find parameter $\tau^{(n)}$ through line minimization.

6. Update the control variable through (3.10); $n = n + 1$.

7. Go back to 2.

The loop continues until the optimality condition (3.11) is approximately satisfied, i.e., $\nabla \mathcal{J}_\eta(\mathbf{f}^{(n)}) \approx 0$. More precisely, the iterations end as soon as $\|\nabla \mathcal{J}_\eta(\mathbf{f}^{(n)})\|$ becomes less than a prescribed tolerance. In practice, a upper bound is also defined on the number of iterations in the sense that after a prescribed number of iterations the optimization stops even if the optimality condition is not satisfied.

In this work, a pseudo-spectral method (see §3.2.1) is used to solve Navier–Stokes and adjoint equations numerically. Since the adjoint equation is expressed in terms of the Fourier space representatives and the boundary conditions are doubly periodic, the Fourier spectral method is arguably the most efficient way to solve it. Time integration is performed with a Krylov subspace method (see §3.2.1). As was mentioned above, the parameter τ is evaluated by a line search method (see §3.2.3). This method uses successive evaluations of the cost functional. Each evaluation of the cost functional requires solving the Navier–Stokes equation. Usually between 15 to 25 cost functional evaluations are required for each line minimization. Therefore, it turns out that the most costly part of the above algorithm is evaluation of the parameter τ.

Before applying this method to the problem of KLB theory, we will comment on the two essential questions associated with any optimization method: Convergence and Uniqueness.

- **Convergence** Note that the criterion for the convergence of the algorithm is the optimality condition $\nabla \mathcal{J} \approx 0$. However, it is known that this condition holds in saddle points in addition to minima (and maxima). Therefore, convergence of the algorithm is not necessarily indicative of reaching to a minimum.

- **Uniqueness** The results are non-unique in two ways. On one hand, the problem is non-convex. Because of the non-convex nature of the governing equations (i.e. NSE) there might be several local minima of the cost functional (see figure 3.1). Therefore, the algorithm might converge to a local minimum. The trivial solution is to run the algorithm from several initial guesses and compare the calculated minima. On the other hand, the map between the velocity fields and the energy spectrum is not injective. As a result, there there are (infinitely) many velocity fields with the same energy spectrum. This is clear from the definition of the energy spectrum (3.4) since it only depends on the amplitude of the velocity and is blind to the phase structure of the field.

3.2 Computational Method

So far, we have defined a cost functional such that its minimum corresponds to a flow with KLB scaling of the energy spectrum. Any gradient-based minimization method will in theory reveal this minimum through an iterative process (i.e. algorithm 3.1.1). On the other hand, the gradient of the cost functional is the solution of the adjoint system (3.20). Since the solutions of the adjoint equation are not in general known in a closed form, a numerical solution of that equation is required. This requires a solution of the NSE (3.3) since these solutions appear as coefficients in adjoint system. Therefore, for each evaluation of the gradient of the cost functional, the NSE and the appropriate adjoint equation must be solved. In the following, the computational methods used for solving these equations are briefly described and references are presented for further details.

3.2.1 Descritization and Time Integration

Descritize the physical domain $\mathbb{T}^2 = [0, 2\pi] \times [0, 2\pi]$ into an $N \times N$ uniform grid (N grid points in each driction). The velocity field is evaluated at each grid point by $\mathbf{u}(x_m, y_n)$ where $m = 0, 1, \cdots, N-1$, $n = 0, 1, \cdots, N-1$, $x_0 = y_0 = 0$ and $x_{N-1} = y_{N-1} = 2\pi$. Consider the following PDE

$$\partial_t \mathbf{u} = F(\mathbf{u}), \tag{3.22a}$$

$$\mathbf{u}(0) = \mathbf{u}_0, \tag{3.22b}$$

where $F(\mathbf{u})$ is the according descritization of the right hand side of either (3.3) or (3.20) with the corresponding initial and boundary value conditions. In each case the first and second order derivatives of the velocity field (or the adjoint variable) appear. Here, the spatial derivatives are taken by a *pseudo spectral* method as follows. For a vector field $\mathbf{u}$ with $u_i : \mathbb{T}^2 \to \mathbb{R}^2$ where $\mathbb{T}^2$ is the doubly periodic box, the Fourier transform of the partial derivatives and the Laplacian operator satisfy

$$\widehat{\frac{\partial u_i}{\partial x_j}}(\mathbf{k}) = \hat{\imath} k_j \hat{u}_i(\mathbf{k}), \tag{3.23}$$

and

$$\widehat{\Delta u_i}(\mathbf{k}) = -k^2 \hat{u}_i(\mathbf{k}), \tag{3.24}$$

for $i, j = 1, 2$ and $\mathbf{k} = \langle k_1, k_2 \rangle$. These identities are exact. The approximation is in the number of Fourier modes (or number of terms in the Fourier series) which are used to approximate the vector field.

Note that the non-linear term in NSE, i.e. $\mathbb{P}(\mathbf{u} \cdot \nabla \mathbf{u})$ turns into a convolution product under Fourier transform which in its discrete form appears

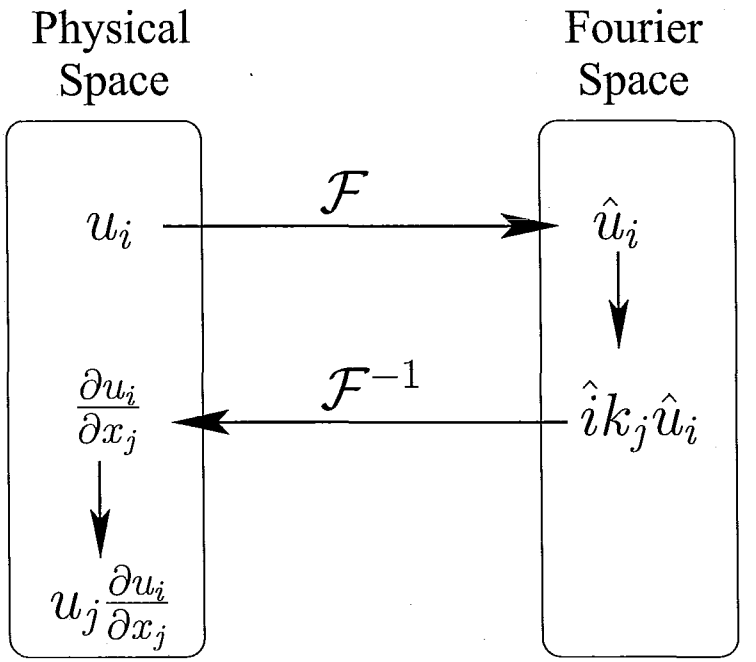

Figure 3.2: Calculating the non-linear term in Navier–Stokes equation by a pseudo-spectral method. The symbols $\mathcal{F}$ and $\mathcal{F}^{-1}$ stand for forward and inverse Fourier transforms respectively.

in equation (2.4) as a finite sum. In order to get around the computational cost and truncation error of calculating this sum, one can use the following trick. Instead of calculating the nonlinear term $u_j(\mathbf{x})\frac{\partial u_i}{\partial x_j}(\mathbf{x})$ in Fourier space or in physical space, we calculate the derivatives $\frac{\partial u_i}{\partial x_j}$ in Fourier space using the above-mentioned formula while the product is carried in physical space. In short, the velocity field must be transformed to Fourier space. Then the derivatives are calculated and the result is transformed back to physical space by an inverse Fourier transform. Finally, the product between the velocity field and its derivatives are calculated in physical space. This process is illustrated in figure 3.2. Similar algorithm is used to calculate the term $\left[\nabla \mathbf{u}^* + \nabla \mathbf{u}^{*^T}\right] \mathbf{u}$ (which is *linear* with non-constant coefficients) in the adjoint system (3.20).

Using the pseudo spectral method described above one can calculate the right hand side (RHS) of equation (3.22). This leaves us with a system of first order ordinary differential equations (ODE) in time. Consider the linearized form of (3.22) around state $\mathbf{u}_0$,

$$\partial_t \mathbf{u} = F(\mathbf{u}_0) + A(\mathbf{u} - \mathbf{u}_0) + R(\mathbf{u}), \tag{3.25a}$$

$$\mathbf{u}(0) = \mathbf{u}_0, \tag{3.25b}$$

where $A \triangleq DF(\mathbf{u}_0)$ is the Jacobian of RHS and therefore a linear operator.

In the case of equation (3.3), the operator A is the right hand side of NSE linearized around state $\mathbf{u}_0$ and in the case of the adjoint equation (3.20), A is the same as the right hand side of the adjoint equation evaluated at $\mathbf{u}_0$ since the equation is linear. The remainder term $R(\mathbf{u})$ is the non-linear part of the right hand side defined as $R(\mathbf{u}) = F(\mathbf{u}) - F(\mathbf{u}_0) - A(\mathbf{u} - \mathbf{u}_0)$. Note that the remainder term for linear equations (such as the adjoint equation) is zero.

The exact solution of (3.25) satisfies the integral equation

$$\mathbf{u}(t) = \mathbf{u}_0 + (e^{tA} - I)A^{-1}F(\mathbf{u}_0) + \int_0^t e^{(t-\tau)A}R(\mathbf{u}(\tau))\ \mathrm{d}\tau. \tag{3.26}$$

In general there are no closed solutions to this integral equation, however, assuming $R = 0$, the solution is immediate. Since $e^{tA} = \sum_{n\geq 0}(t^n/n!)A^n$, this solution can be written as

$$\mathbf{u}(t) = \mathbf{u}_0 + \sum_{n\geq 1}\frac{t^n}{n!}A^{n-1}F(\mathbf{u}_0). \tag{3.27}$$

In order to achieve a highly accurate solution (desirable for turbulence studies), one needs to calculate the above series up to a relatively large number of terms. It is computationally expensive to calculate the powers of the matrix A directly. Diagonalizing A does not save much computational cost either. Therefore, an alternative method should be acquired in order to calculate the above power series. Here, we use *Krylov subspaces* method. This method is described briefly in the following. The reader is referred to [8] and [32] for more details about the convergence rate and stability of the scheme.

A K-dimensional Krylov subspace is the span of vectors $\{v_1, v_2, \cdots, v_K\}$ which are calculated through an *Arnoldi process* [8] from matrix A and vector $F(\mathbf{u}_0)$. The Krylov vectors satisfy

$$span\{v_1, v_2, \cdots, v_K\} = span\{F(\mathbf{u}_0), AF(\mathbf{u}_0), \cdots, A^{K-1}F(\mathbf{u}_0)\}. \tag{3.28}$$

Define the $N \times K$ matrix V such that each of its columns is a Krylov vector. Then $V^TV = I_K$ where I_K is the $K \times K$ identity matrix. Define the $K \times K$ matrix $H \triangleq V^TAV$. Then

$$A^n = VH^nV^T. \tag{3.29}$$

Suppose that the diagonal form of H is given by $H = E\Lambda E^{-1}$ where Λ is the diagonal matrix [1]. One can calculate this through a QR algorithm [16]. Then exponents of A can be written as $A^n = VE\Lambda^nE^{-1}V^T$. Since Λ is diagonal, no matrix multiplications are required for calculating its exponents.

Substituting $VE\Lambda^{n-1}E^{-1}V^T$ for A^{n-1} in (3.27), we get

$$\tilde{\mathbf{u}}(t) = \mathbf{u}_0 + VE(e^{t\Lambda} - I)\Lambda^{-1}E^{-1}V^TF(\mathbf{u}_0), \tag{3.30}$$

[1] It is easy to show that the matrix H is upper Hessenberg.

where $\sim$ denotes an approximate solution. Computaion of $e^{t\Lambda}$ and Λ^{-1} requires no matrix multiplications since Λ is diagonal.

Remark: Note that the most costly part of these computations is diagonalization of H. Since matrix H is much smaller than the original matrix A, it is much less expensive to diagonalize H than to diagonalize A. This is the main motivation for using Krylov subspaces. For instance, in the simulations of chapter 4, A is a 1024×1024 matrix while H is a 15×15 matrix!

So far we have assumed that the remainder term $R(\mathbf{u})$ is identically zero. In the case that it is non-zero (e.g. in NSE), we should somehow approximate it in order to achieve a closed solution. In [8], it has been shown that the linear solution obtained from (3.30) can be used instead of $\mathbf{u}$. That is to assume $R(\mathbf{u}(\tau)) \approx R(\mathbf{u}^L(\tau))$ where $\mathbf{u}^L$ is calculated by (3.30). Then expand $R(\mathbf{u}^L(\tau))$ as the power series

$$R(\mathbf{u}^L(\tau)) \approx \sum_j \mathbf{r}_j \tau^j \tag{3.31}$$

where $\mathbf{r}_j$ is a vector of length N which is evaluated in other to fit the sum to the values of $R(\mathbf{u}^L(\tau))$ over some set of points in time. Substituting the above power series in the exact solution (3.26), we get

$$\begin{aligned}\tilde{\mathbf{u}}(t) = \mathbf{u}_0 &+ VE(e^{t\Lambda} - I)\Lambda^{-1}E^{-1}V^T F(\mathbf{u}_0) \\ &+ VE\sum_j \left(\int_0^t e^{(t-\tau)\Lambda}\tau^j \, \mathrm{d}\tau\right) E^{-1}V^T \mathbf{r}_j,\end{aligned} \tag{3.32}$$

where the exponential $e^{(t-\tau)A}$ is again approximated by the Krylov subspaces method as described above, i.e. $e^{(t-\tau)A} = VEe^{(t-\tau)\Lambda}E^{-1}V^T$.

The absolute numerical error is defined as the maximum norm of the difference between the time derivative of the above approximate solution and the RHS evaluated at $\tilde{\mathbf{u}}(t)$, i.e. $\delta = t\|\partial_t\tilde{\mathbf{u}} - F(\tilde{\mathbf{u}})\|_\infty$. The numerical solution is acceptable if the relative error is less than a prescribed tolerance ϵ, i.e.

$$e = \frac{\delta}{\|\mathbf{u}_0\|_2} < \epsilon \tag{3.33}$$

Once this condition is satisfied the numerical method has converged and one step of the time integration has been carried out. Next time steps are calculated similarly.

3.2.2 Parallelization

The numerical method used to solve NSE and the adjoint equation was described in the previous section. In each iteration of the algorithm 3.1.1, NSE is solved forward in time (step 2). The solutions of NSE are used as coefficients in the adjoint equation which must be solved backward in time (step

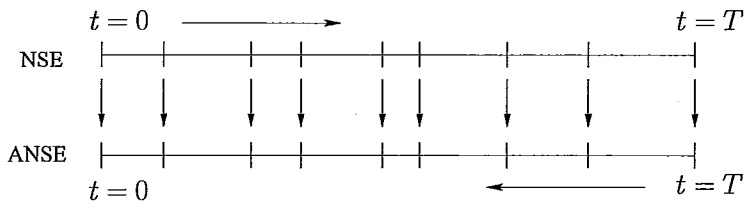

Figure 3.3: ANSE stands for adjoint Navier–Stokes equation. NSE is solved forward in time and its solutions are used in ANSE. Note that since the code is adaptive in time the time steps are not uniform.

3). These two steps are illustrated in figure 3.3. In addition, NSE is solved for several times (between 10 to 20 times) in order to perform the line minimization in step 5 (Line minimization algorithm is described in §3.2.3). Since for turbulence simulations relatively high resolutions are required ($N = 1024$ in our case), solving the above-mentioned equations on a single processor leads to an impractical execution time (Note that NSE must be solved for several times at each iteration). Therefore, we have parallelized the time integrations as follows.

A Massage Passing Interface (MPI) approach is adopted for parallelization. The physical domain is divided into horizontal regions in y-direction as illustrated in figure 3.4. For each region, a single processor is specified to carry out the computations related to that region. Computations are performed locally wherever possible. The only significant non-local computation is due to calculation of the Fourier transform since it requires the data from all regions. The standard MPI FFTW 2.1.5 [10] is used for computing the Fourier transform.

Let T_1 and T_p be the CPU time required to integrate NSE using one processor and p processors respectively. The speedup defined as

$$S_p = \frac{T_1}{T_p}, \tag{3.34}$$

is ideally equal to p. This means that by doubling the number of processors the execution time decreases to half of its initial value. This situation rarely happens in practice. The speedup is usually less than p. The reason is mostly due to the required communications among processors. It happens quite often that a processor needs to read the value of a variable from another processor and therefore needs to "communicate" with that processor. If the number of processors is too large compared to the size of the problem, these communication time dominates the computation time and therefore cancels the speedup obtained from increasing the number of processors. Therefore, in order to choose the proper number of processors, it is essential to analyze the speedup of the parallel code. In the following, we present the results of several experiments that have been conducted to analyze the speedup of the code.

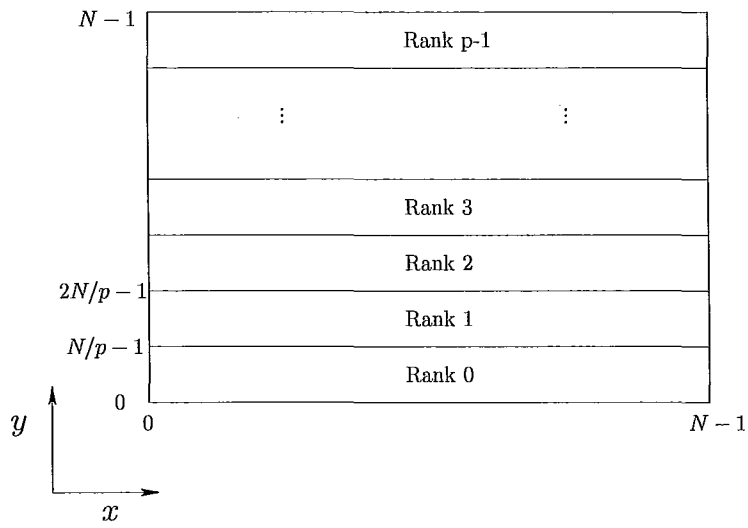

Figure 3.4: $N \times N$ grid points divided among p processors. Rank refers to the label of the processor by which it is called.

Several parameters (e.g., viscosity, domain size, initial condition, etc.) are present in the equations. Most of these parameters are the same for following experiments in order to make a reliable comparison between the results. For a fixed problem size N^2 (equal to the number of grid points), the CPU time using various number of processors p is measured and the results are compared. We use the parallel code to solve both NSE and the adjoint system, however, the scaling analysis are conducted only on NSE. Recall that for each iteration of the optimization algorithm, the adjoint equation is solved only once while NSE is solved between 10 to 20 times. This means that more than 95% of the execution time belongs to solving NSE. Therefore, it is reasonable to choose the optimum number of processors based on their performance in solving NSE.

The scaling analysis are conducted for four different number of grid points N^2 and viscosity ν. These quantities are reported in table 3.1 for each case. In all cases NSE is integrated over the time interval $t \in [0, 1]$. The physical domain is the $[0, 2\pi] \times [0, 2\pi]$ torus. For each case the total CPU time[2] is measured in seconds when $p = 1, 2, 8, 16, 32$, 64 and 128 processors are used. All computations are performed on SHARCNET[3] cluster named `requin` which uses *Opteron* processors at 2.6 GHz with 8.0 GB memory.

The results are plotted in figure 3.5a. For each experiment the CPU time is normalized by T_1 (=the CPU time when one processor is used).

The other important factor in parallel programming is the *efficiency* of the

[2]Here, total CPU time refers to the time needed to finish the computation.
[3]Shared Hierarchical Academic Research Computing Network

Table 3.1: Parameters of the scaling analysis.

	Exp#1	Exp#2	Exp#3	Exp#4
N	256	512	1024	1024
ν	4.8×10^{-4}	4.8×10^{-4}	4.8×10^{-4}	6.0×10^{-5}

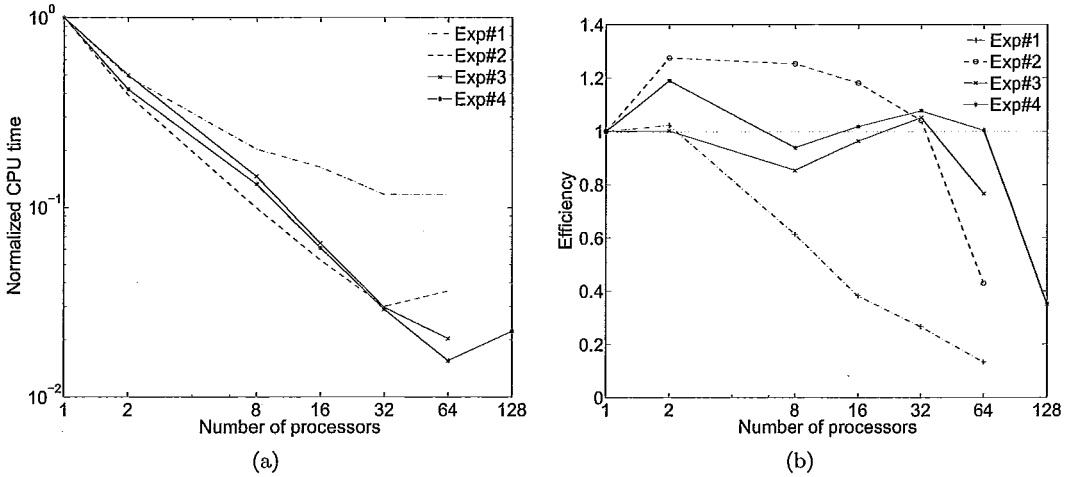

Figure 3.5: The CPU time normalized by the CPU time when one processor is used (a) and the efficiency of the parallel algorithm (b).

computations. Efficiency is defined as

$$E_p = \frac{T_1}{pT_p} \tag{3.35}$$

and determines that how well-utilized the processors are in computations. In other words it shows whether it is worth increasing the number of processors. An efficiency higher than 50% is usually acceptable. Figure 3.5b shows the efficiency of the parallelization in above-mentioned experiments.

The above scaling analysis shows that the speedup is almost linear (or even super-linear) except for $N = 256$. This is better shown in figure 3.5b where the efficiency is almost 100% or higher. This high efficiency is not surprising considering the simple geometry of the problem which makes it quite efficient for parallelization with least number of processor communications. Moreover, note that in addition to reducing the number of floating-point operations (FLOP) per processor, increasing the number of processors may allow each CPU to use its cache memory. The cache memory is faster than the RAM memory which takes over when smaller number of processors are used. However, as expected, beyond some point increasing the number of processors does not decrease the CPU time.

In all simulations of chapter 4, $N = 1024$ and $\nu = 6.0 \times 10^{-5}$ which coincides with Exp#4. In that experiment, the speedup is maximum when $p = 64$

and the corresponding efficiency is almost 100%. Therefore, we will use 64 processors on `requin` in all simulations hereafter.

3.2.3 Line Minimization

It was mentioned that the computationally most expensive part of our optimization algorithm is the line minimization. In this section, the line minimization algorithm is described. For further details and some alternative methods, refer to [27].

The solutions of the adjoint equation determine the descend direction $-\nabla\mathcal{J}$. However, it is not known how far in that direction the control variable (here the forcing) should be move in order to give a substantial reduction in the cost functional. More precisely, it is known that there is $s > 0$ such that $\mathcal{J}(\mathbf{f}+\tau\nabla\mathcal{J}) \leq \mathcal{J}(\mathbf{f})$ for any $\tau \in (-s, 0)$. However, the "best" value of τ is not generally known. In general, it is computationally too expensive to identify the optimal value of τ. In some applications, it is enough to try some negative values for τ and then choose the one that gives rise to the largest decrease in the cost functional. However, in some applications (such as the present problem) where the cost functional is highly sensitive, a more sophisticated method is required to evaluate an optimal value for τ. This can be formulated as minimization of the function $\mathcal{G}(\tau) \triangleq \mathcal{J}(\mathbf{f} + \tau\nabla\mathcal{J})$ respect to variable τ for fixed $\mathbf{f}$ and $\nabla\mathcal{J}$:

$$\min_{\tau\in\mathbb{R}^-} \mathcal{G}(\tau). \tag{3.36}$$

There are various methods to solve the above minimization problem. The method used here is the *brent* method. It requires an interval in which the minimum exists to be given. To find this interval the following bracketing algorithm is used.

Algorithm 3.2.1.
Choose $\alpha < 0$, $\rho \in (0, 1)$ and $c \in (0, 1)$;
repeat until $\mathcal{G}(\alpha) \leq \mathcal{J}(\mathbf{f}) + c\alpha(\mathbf{f}, \nabla\mathcal{J})_U$
$\ldots\alpha \leftarrow \rho\alpha$;
end (repeat)
Set $s = -\alpha$;

The above algorithm is listed under `mnbrack` with full details in [40]. While the interval $(-s, 0)$ in which the minimizer of $\mathcal{G}$ exists is known one can apply the brent method. The brent method is a fairly complicated algorithm. In the following a simplified version of this method is described. The reader is referred to [40, 27] for a detailed implimentation and discussion.

For the first step of the brent method set $a \leftarrow 0$ and $c \leftarrow -s$. Choose an arbitrary point b between a and c, say the midpoint $b \leftarrow (a + c)/2$. Find

the parabola which passes the points $(a, \mathcal{G}(a))$, $(b, \mathcal{G}(b))$ and $(c, \mathcal{G}(c))$. Assume that the minimum of this parabola occurs at b_0. Thanks to the fact that the minimizer of $\mathcal{G}(\cdot)$ is between a and b, either $b_0 \in (c, b)$ or $b_0 \in (b, a)$. If $b_0 \in (c, b)$, redefine a, b and c as follows
$a \leftarrow b$,
$b \leftarrow b_0$,
$c \leftarrow c$,
otherwise
$c \leftarrow b$,
$b \leftarrow b_0$,
$a \leftarrow a$.
This ensures that the new value of b is closer to the minimizer of $\mathcal{G}(\cdot)$ than the previous value of b [40]. By continuing this procedure for the updated values a, b and c, the value of b eventually converges to the minimizer of $\mathcal{G}(\cdot)$.

It is evident that the brent method requires several evaluations of the function $\mathcal{G}$ which in turn requires evaluation of the functional $\mathcal{J}$. Recall for each functional evaluation, it is required to solve the Navier–Stokes equation. This increases the computational cost of the optimization and justifies the necessity of the code parallelization as described in §3.2.2

Chapter 4

Results

In this chapter, the optimal control method developed in §3.1 is applied to 2-D turbulence in order to study the effect of forcing on the scaling laws of the energy spectrum. The results are presented and discussed in details. Equations (3.3) and (3.20) are solved with $\nu = 6.5 \times 10^{-5}$ using 1024^2 Fourier modes. The aliasing effect of the nonlinear term is removed by the 2/3 rule. To reduce the computational time, the initial condition, $\mathbf{u_0}(\mathbf{x})$, is a fully-developed turbulent field forced by a mono-scale forcing (see figure 4.1). The initial guess in step 1 of the algorithm 3.1.1 is zero, i.e. $\mathbf{f}^{(0)} \equiv \mathbf{0}$. The constants of proportionality in equation (3.5) are $C_1 = 1.18$ and $C_2 = 64.00$. These values are chosen in order to retrieve a continuous target energy spectrum, $E_0(k)$, with the total energy close to the total energy of the initial condition. The weight function in equation (3.6) is $w(t,k) = k^6\sqrt{t/T}$ in order to normalize the error over different wave-numbers and also to put more emphasis on the contribution of the error near $t = T$, where the termination time is $T = 4$. Here, the penalization parameter η in (3.21) is equal to zero.

Based on the types of forcing, the results are divided into two parts as follows:

i. Full-band forcing (§4.1)

ii. Band-limited forcing (§4.2)

In case (i) the forcing is allowed to be active at any wavenumber. Therefore, it does not necessarily respect the inertial range assumption of the KLB theory since it may add (or remove) energy and enstrophy into (from) the cascading wavenumbers. We show, however, that the inertial interactions (responsible for the cascades) still dominate the flow dynamics. This forcing is physically more realistic than the (theoretically interesting) monoscale forcing. For instance, [41] present a model of the atmospheric flow in which the forcing is due to temperature gradients and active over a portion of the enstrophy cascade.

In case (ii) the forcing is non-zero only at a few intermediate wavenumbers (i.e. $k \in (k_2^e, k_1^z)$) and a few small wavenumbers (i.e. $k \in [1, k_1^e)$) (see figure 2.5). Therefore, the scalings of the energy and enstrophy cascades are exclusively due to inertial (triad) interactions. This forcing resembles the classical band-limited forcing used in most numerical simulations. However, we do not define the forcing *a priori*, but calculate it through the optimization. Our forcing may be non-zero at a few small wavenumbers in order to allow the large scale energy dissipation, if necessary.

In terms of the optimal control setting, in case (i) the only restriction on the forcing is to be square integrable. In other words the cost functional ($\mathcal{J}$) is minimized over the function space $\mathcal{U} = L^2([0,T]; L^2(\mathbb{T}))$. While in case (ii), the control space is

$$\mathcal{U} = \left\{ \mathbf{f} \in L^2([0,T]; L^2(\mathbb{T})) \,:\, \hat{\mathbf{f}}(t,\mathbf{k}) = \mathbf{0},\ |\mathbf{k}| \in [k_1^e, k_2^e] \cup [k_1^z, k_2^z] \right\}. \tag{4.1}$$

In addition to the two cases mentioned above, the enstrophy cascade in the absence of the energy cascade is studied in §4.3.

4.1 Full-band Forcing

The parameters that determine the scaling ranges are $k_1^e = 2$, $k_2^e = k_1^z = 20$ and $k_2^z = 200$. Figure 4.1 shows that the optimal control method gives the spectral slopes predicted by KLB theory. This energy spectrum remains stationary on the time interval $\frac{1}{2}T \leq t < T$ where $T = 4 \approx$ two eddy turnover times. In figure 4.2, the instantaneous vorticity fields produced by a monoscale forcing (left) and the optimal forcing (right) are compared. It is obvious that the optimal forcing produces more small scale, filamentary structures.

We now present some properties of this optimal forcing. An interesting quantity is the contribution of the forcing to the energy spectrum of the velocity field. This quantity is defined by

$$F(t,k) = \int_{|\mathbf{k}|=k} \Re\{\hat{\mathbf{f}}(t,\mathbf{k}) \cdot \overline{\hat{\mathbf{u}}(t,\mathbf{k})}\}\, \mathrm{d}S(\mathbf{k}), \tag{4.2}$$

and indicates whether the forcing injects energy into (if positive) or removes energy from (if negative). Figure 4.3 shows that the optimal control injects energy into the system mostly at wave-number $k = 20$ (i.e. the wave-number at which the spectral slope changes from $-5/3$ to -3 , see figure 4.1). This is a non-trivial result since the control method allows the forcing to act over the whole wavenumber range. The energy injection by forcing decays to zero exponentially for $k \geq 20$. For $1 \leq k \leq 6$ the optimal forcing removes energy from the system which creates a sink of energy in large scales. Since energy is

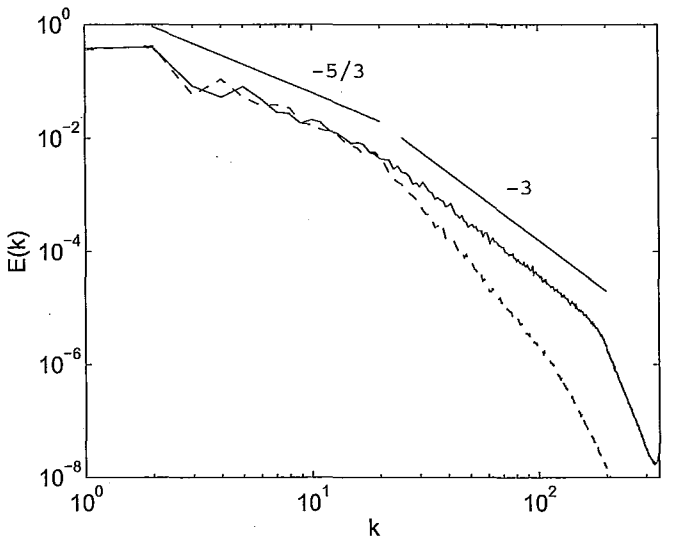

Figure 4.1: The energy spectrum of the initial condition (- - -) and the energy spectrum (resulted from the optimal full-band forcing) at $t = \frac{3}{4}T$ (—). The straight lines represent the -5/3 and -3 slopes.

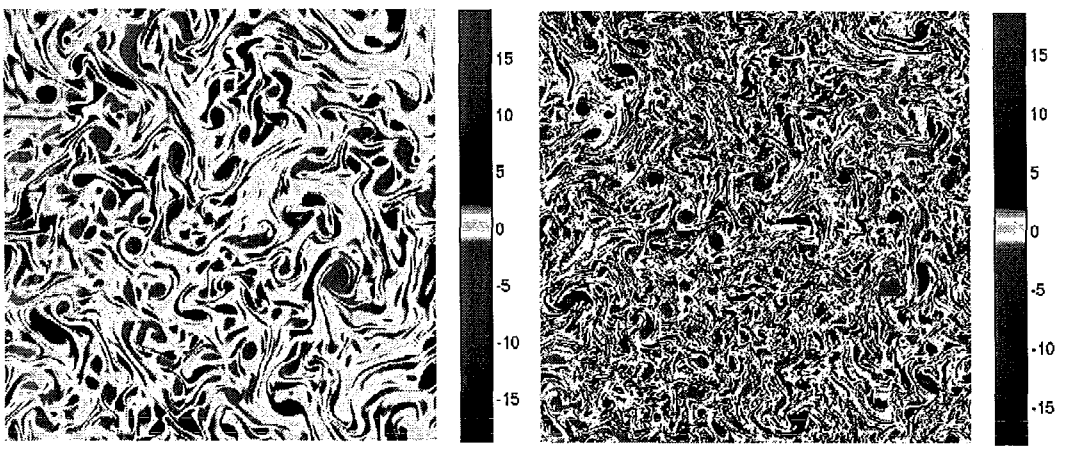

(a) (b)

Figure 4.2: Vorticity fields resulting from the band-limited forcing (a) and the optimal full-band forcing (b)

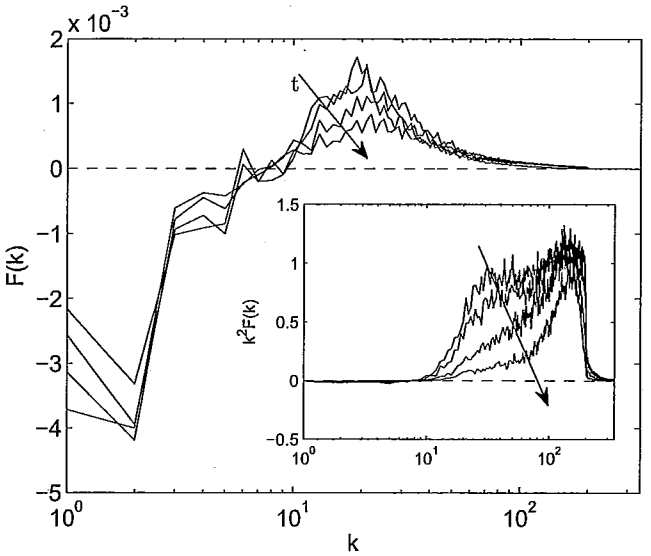

Figure 4.3: The energy is mostly injected at $k = 20$ by the external forcing. Different lines correspond to different time slices. The inset shows the corresponding enstrophy injection.

transferred to larger scales, a mechanism to dissipate it is necessary in order to reach a statistically stationary state in forced 2-D turbulence. Moreover, Tran and Shepherd [36] proved that the presence of a large scale sink of energy is necessary in order to obtain the dual cascades with $-5/3$ and -3 slopes when the forcing is monoscale or band-limited. In the present case where the forcing is full-band the large scale energy dissipation seems to be necessary, and is produced automatically by the optimal control method.

The energy spectrum of the forcing which is defined by

$$E_f(t,k) = \frac{1}{2}\int_{C(k)} |\hat{\mathbf{f}}(t,\mathbf{k})|^2 \, \mathrm{d}S(\mathbf{k}),$$

is plotted in figure 4.4 for several time slices. It shows that the forcing is active on a wide range of scales which means that the energy and enstrophy cascades are not inertial ranges. The forcing decays to zero as time increases (also consistent with figure 4.3). This decay is an artifact of the control algorithm. Since we start with a zero initial guess (i.e. $\mathbf{f}^{(0)} \equiv \mathbf{0}$) and the gradient of the cost functional is zero at $t = T$ (see equation (3.20)), the forcing remains equal to zero at $t = T$ for all iterations, i.e. $\mathbf{f}^{(n)}(T,\mathbf{x}) \equiv \mathbf{0}$.

It is also necessary to examine the dynamical properties of the flow generated by the optimal forcing since one can generate a random phase vector field with -3 (or -5/3) energy spectrum (and no dynamics or cascades). Therefore, we need to check that the the resulting flow is dynamically active. As mentioned earlier, the triad interactions determine the dynamics of the energy and

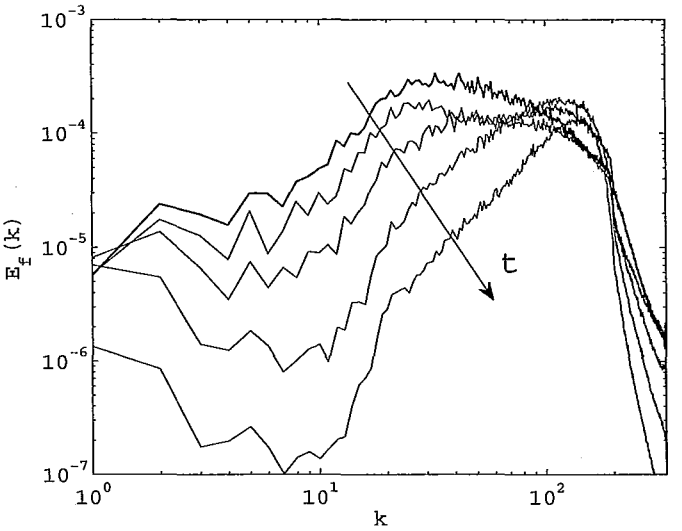

Figure 4.4: The energy spectrum of the forcing at different time slices. As time increases the energy level of the forcing decreases to zero.

enstrophy cascades associated with the nonlinear term in the Navier-Stokes equation. In 2-D, they transfer most of the energy to larger scales and most of the enstrophy to smaller scales. Since our optimal forcing is non-zero on the cascading ranges, it can significantly affect these transfers. In the following, we will show that the triad interactions still dominate the dynamics of the flow in the presence of the optimal control forcing.

For each three wave vector triad $\mathbf{k}$, $\mathbf{p}$ and $\mathbf{q}$, we use the method introduced in [24] to calculate the the energy transfer function, $T_{\mathbf{kpq}}$. The enstrophy transfer function, $S_{\mathbf{kpq}}$, is related to energy transfer function by $S_{\mathbf{kpq}} = k^2 T_{\mathbf{kpq}}$ where $k = |\mathbf{k}|$. The positive values of the quantity $T_{\mathbf{kpq}}$ ($S_{\mathbf{kpq}}$) correspond to energy (enstrophy) transfer rate *into* mode $\mathbf{k}$ due to interactions with modes $\mathbf{p}$ and $\mathbf{q}$. Similarly, the negative values of these quantities correspond to the energy and enstrophy transfer rates *out* of mode $\mathbf{k}$.

We simplify the transfer functions (and make them consistent with the statistical KLB theory) by averaging over one of the wave-vectors and defining

$$T_{\mathbf{kp}} = \sum_{\mathbf{q}} T_{\mathbf{kpq}}.$$

Since we consider isotropic turbulence, it is appropriate to average over angles in wave-number space. This further simplifies the calculations and leads to the following definition of the energy transfer function in terms of two wave-numbers

$$T_{kp} = \int_{|\mathbf{k}|=k} \int_{|\mathbf{p}|=p} T_{\mathbf{kp}} \, \mathrm{d}S(\mathbf{p}) \, \mathrm{d}S(\mathbf{k}). \tag{4.3}$$

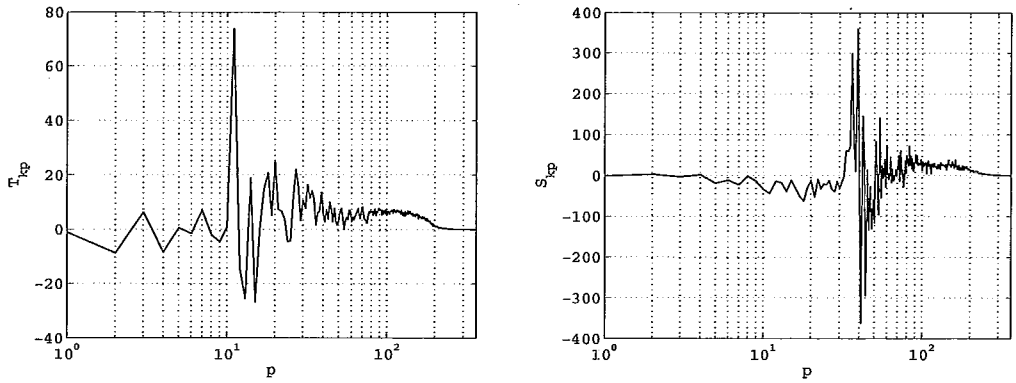

(a) T_{kp}, $k = 10$. (b) S_{kp}, $k = 40$

Figure 4.5: The time averaged energy (T_{kp}) and enstrophy (S_{kp}) transfer functions.

The two-wave-number enstrophy transfer function, S_{kp}, is defined similarly, and is related to T_{kp} by $S_{kp} = k^2 T_{kp}$.

The time-averaged energy and enstrophy transfer rates are plotted in figure 4.1 for the fixed wave-number $k = 10$ (for energy) and $k = 40$ (for enstrophy) and in terms of p. The data is noisy since the transfer functions are averaged over a relatively short time interval ($0 \leq t \leq 4$). However, some interesting features may be observed. In a neighbourhood of $k = 40$, the enstrophy transfer function is positive for $p < k$ while it is negative for $p > k$. Similar behaviour is observed for wave-numbers $25 \leq k \leq 150$ (not presented here). This shows that the enstrophy is mostly transferred to smaller scales on this range of wave-numbers. On the other hand, the energy transfer function is negative for $p < k$ and positive for $p > k$ which shows an energy transfer to larger scales. These results provide evidence that the optimal forcing respects the directions of the energy and enstrophy cascades.

There is another independent way of checking the direction of energy and enstrophy cascades. In their proof, Gkioulekas and Tung [15] present a sufficient condition for the existence of the upscale energy and downscale enstrophy cascades in a statistically stationary state. This condition is

$$G(t,k) = 2\nu k^2 E(t,k) - F(t,k) > 0, \tag{4.4}$$

where $E(t,k)$ is the energy spectrum as defined in (3.4) and $F(t,k)$ is the energy injected (or removed) by the forcing calculated through (4.2). Note that the inequality holds for band-width-limited forcings and any wave-number, k, outside the band-width of the forcing since $F(t,k) = 0$ for these modes. Figure 4.6 shows the quantity $G(t,k)$ for the optimal forcing and for several time slices. Note that the time dependence of the energy spectrum can be eliminated since a statistically steady state is considered, however, $F(t,k)$ is

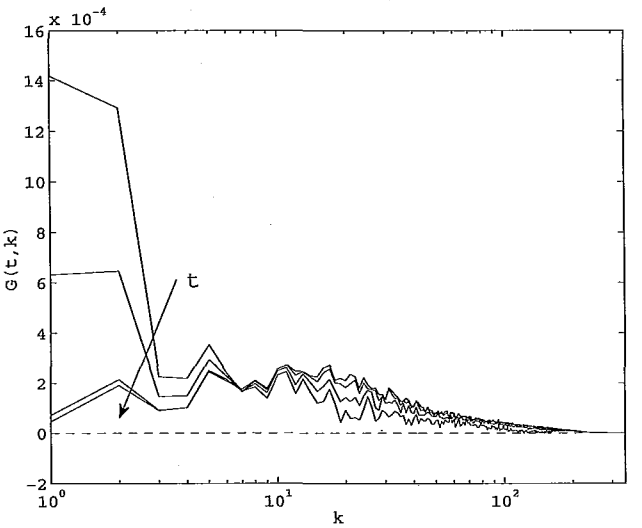

Figure 4.6: The fact that $G(t,k)$ is positive for all k demonstrates the existence of inverse energy and direct enstrophy cascades. Each curve corresponds to a time slice between $\frac{3}{4}T$ and T. The arrow shows the time increase.

still time dependent. This figure shows that the inequality (4.4) is satisfied and therefore, on average, energy is transferred to larger scales while enstrophy is transferred to smaller scales.

In summary, our results demonstrate the existence of a forcing which is consistent with the predictions of KLB theory (i.e. coexisting cascades of energy and enstrophy with $-5/3$ and -3 spectral slopes). The upscale energy and downscale enstrophy cascades are active under this forcing. However, these cascades are not inertial ranges since the forcing is active on a wide range of scales including the cascade ranges. The forcing injects energy (and enstrophy) mostly around the wave-number at which the slope of the energy spectrum changes from $-5/3$ to -3. Moreover, it automatically removes energy from large scales and produces a statistically steady state.

4.2 Band-limited Forcing

We now confine the forcing to the space of band-limited functions defined in (4.1). Since $k_1^e = 3$, $k_2^e = 18$, $k_1^z = 25$ and $k_2^z = 200$, the forcing is non-zero only for the wavenumbers $k \in [1,2] \cup [19,24]$. Note that conventionally, energy is removed from large scales by Ekman drag or by inverse viscosity. Here, we do not use any energy dissipative mechanisms at large scales. Instead, we simply allow the forcing to be non-zero at largest scales. The forcing may remove the energy from those scales if necessary (As the following results demonstrate,

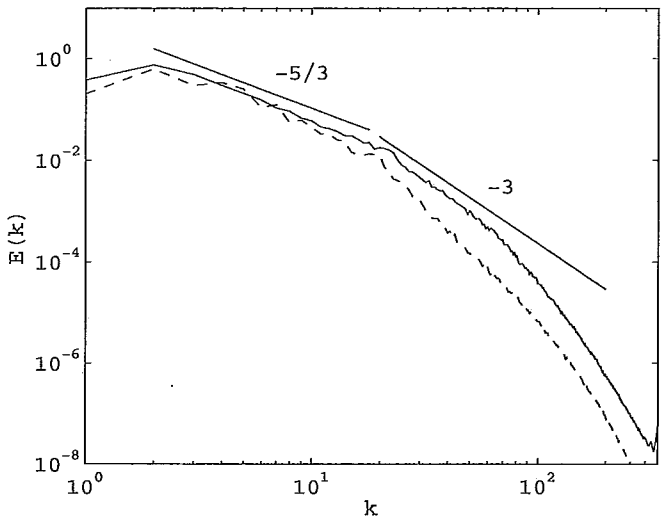

Figure 4.7: The controlled energy spectrum (with band-limited forcing) at $t = \frac{7}{8}T$ (—) and the energy spectrum resulting from the conventional band-limited forcing and inverse viscosity (- - -).

this is in fact the case). The advantage of this method is that the energy injection and large scale energy dissipation are now determined by the control procedure alone: they are not fixed *a priori*.

Figure 4.7 shows the energy spectrum resulting from the band-limited optimal forcing at $t = 3.5$ (Note that in this case $T = 4 \approx$ four eddy turnover times). The energy spectrum follows the KLB scaling law $E \sim k^{-5/3}$ for a decade of wave-numbers and $E \sim k^{-3}$ for a quarter of a decade. As expected, the enstrophy range is extended over a shorter range of wave-numbers compared to the previous case where broad band forcing was used. The energy spectrum resulting from a conventional band-limited forcing and inverse viscosity is given for comparison (dashed line in figure 4.7).

The vorticity field at $t = T$ is presented in figure 4.8a. Figure 4.8b shows the instantaneous non-zero component of $\nabla \times \mathbf{f}$ in physical space. It appears that the forcing is homogeneous and isotropic. However, more careful investigation shows that the forcing is particularly aligned in the favour of enstrophy injection into the system. To see this, note that the total energy and enstrophy injections are given by $\int_{\mathbb{T}} \mathbf{f} \cdot \mathbf{u}\, d\mathbf{x}$ and $\int_{\mathbb{T}} \mathbf{f} \cdot (-\Delta \mathbf{u})\, d\mathbf{x}$ respectively. Therefore, a forcing aligned with velocity injects energy more efficiently while a forcing aligned with $-\Delta \mathbf{u}$ injects enstrophy more efficiently. Figure 4.9 shows the probability distribution function of these alignments over time and space where θ_e and θ_z are respectively the distributions of the angles $\angle(\mathbf{f}, \mathbf{u})$ and $\angle(\mathbf{f}, -\Delta \mathbf{u})$. These figures reveal that the forcing is aligned such that the en-

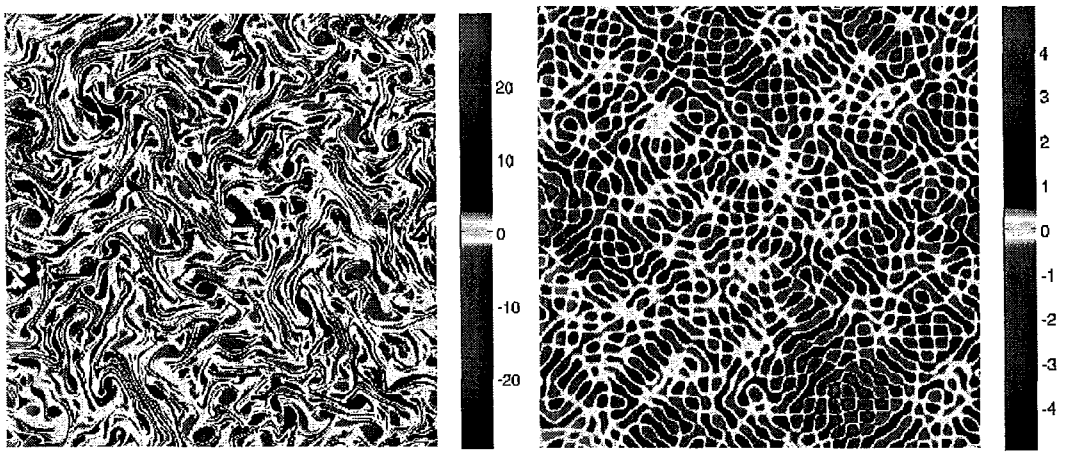

(a) $(\nabla \times \mathbf{u}) \cdot \hat{\mathbf{n}}$ (b) $(\nabla \times \mathbf{f}) \cdot \hat{\mathbf{n}}$.

Figure 4.8: The vorticity field resulted from the optimal band-limited forcing (left) and the curl of the optimal forcing (right) at $t = \frac{7}{8}T$.

strophy injection is relatively more efficient than the energy injection. Note that in the case of a random phase forcing (which is conventional in numerical simulations of 2-D turbulence) there are no preferential alignments of the forcing with the velocity field. Figure 4.10 shows that the time correlation of the optimal forcing defined as $\langle \mathbf{f}(\mathbf{x}, t) \cdot \mathbf{f}(\mathbf{x}, t + \tau) \rangle$ where $\langle\ \rangle$ denotes the average in time and space. The curves are normalized by the correlation at $\tau = 0$. It shows that the time correlation of the optimal forcing is relatively small which resembles the short correlation of the conventional forcing.

The energy contribution to the system from the external forcing (i.e. $F(t, k)$) is shown in figure 4.11. Energy is injected in the wave-numbers $k \in [19, 24]$, while it is removed from largest available scales, i.e. $k \in [1, 2]$. This agrees with the fact that a sink of energy at large scales is a necessary condition for achieving the KLB limit in a finite domain.

Since the forcing is band-limited, the inequality (4.4) is automatically satisfied on the range $k \in [3, 18] \cup [25, +\infty)$. Therefore, the upscale energy and downscale enstrophy fluxes are dominant.

4.3 Enstrophy Cascade with Large-Scale Forcing

In the previous section, we have observed the dual cascade following the KLB scaling. However, the k^{-3} range extended only on a quarter of a decade of wavenumbers. The question is whether this is only due to lack of resolution and entering a region where the energy dissipation due to viscosity becomes significant. One way to answer this question is to increase the resolution which is equivalent to decreasing the viscosity. This is however not the best approach

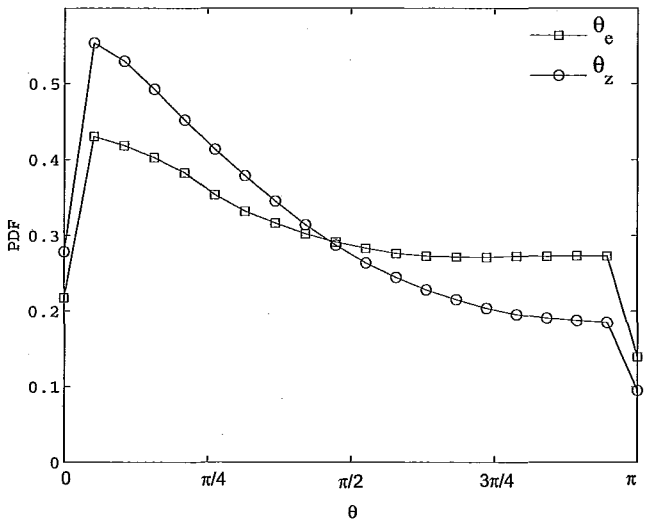

Figure 4.9: The probability distribution function of θ_e (the angle between $\mathbf{f}$ and $\mathbf{u}$) and θ_z (the angle between $\mathbf{f}$ and $-\Delta\mathbf{u}$)

since increasing the resolution increases the computational time significantly. An alternative method is to shift the forcing band to a few smallest wavenumbers. As a result, inverse energy cascade will not exist any more since there are not larger scales than the forcing scale. But then there would be enough modes to resolve an enstrophy cascade up to a decade of wavenumbers. This large scale forcing of 2-D turbulence has been studied extensively [see, e.g., 6, 5, 22]. In all these studies the forcing is either random phase or a simple function of the velocity field. These studies confirm that in the limit of infinite Re-number, the energy spectrum scales as k^{-3}. However, for moderate Re-number flow the spectrum is steeper. To give an estimate, in a 1024^2 resolution the spectrum scales as k^{-4} in []. We show in the following that with a particular choice of forcing the energy spectrum scales as k^{-3} with a resolution of 1024^2. We emphasize, however, that this result can not be immediate carried over to the case of dual cascade since presence of the inverse energy cascade can steepen the enstrophy cascade.

In the following, the enstrophy cascade is controlled over the range $k \in [5, 100]$, the forcing is active over a few first wavenumbers $k \in [1, 4]$ and the time interval is $t \in [0, 4]$. Figure 4.12 shows the resulting energy spectrum in the last iteration. It shows clearly that the energy spectrum now scales as k^{-3} over more than a decade of wavenumbers. We emphasis that the energy spectrum scales (almost) as k^{-4} when a random-phase white-noise-in-time forcing is used.

Figure 4.13 compares the instantaneous vorticity fields resulting from the

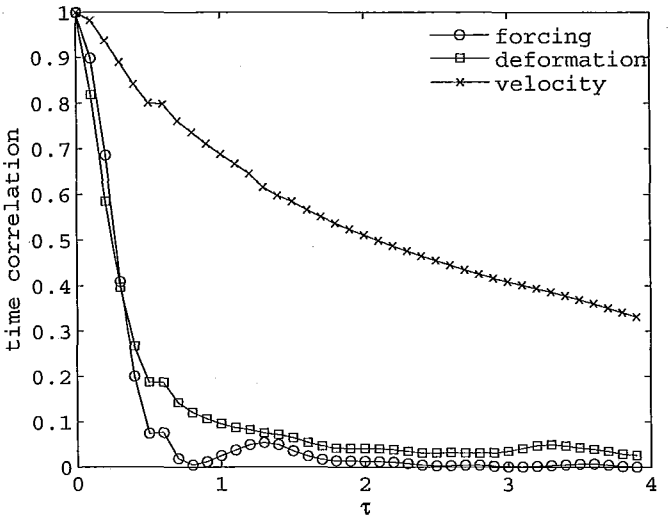

Figure 4.10: Normalized time-correlation functions.

conventional forcing (left) and the optimal forcing (right). The vorticity resulting from the optimal forcing contains relatively finer filamentary structures which are extended over a longer distance in the domain of the flow which is to be expected given its shallower energy spectrum.

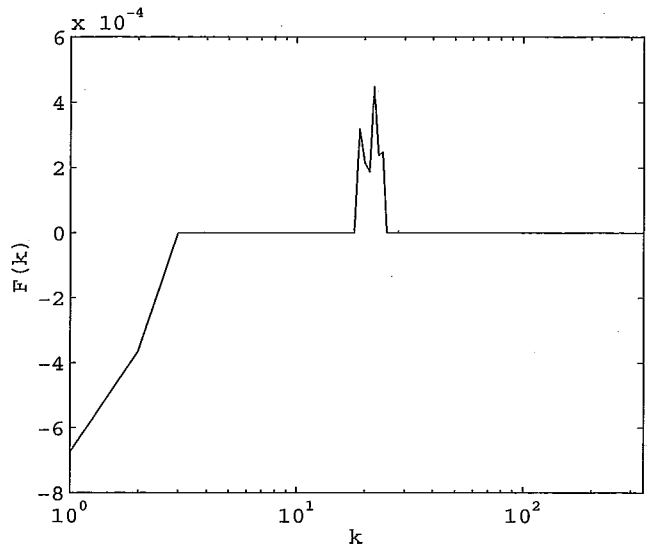

Figure 4.11: Contribution of the forcing to the energy spectrum at $t = \frac{19}{20}T$.

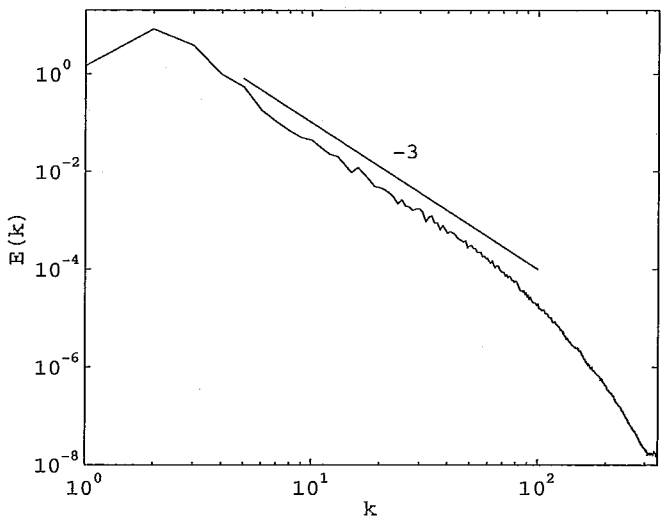

Figure 4.12: Controlled energy spectrum over the enstrophy range.

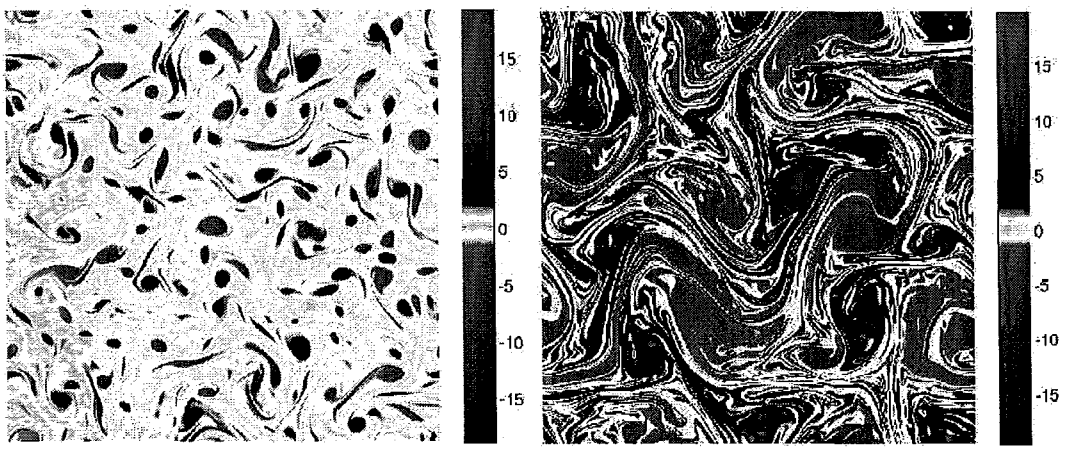

(a) (b)

Figure 4.13: Comparison of the instantaneous vorticity fields with (a) conventional forcing and (b) optimal forcing

Chapter 5

Summary and Conclusion

In this chapter, we summarize the main results and add some concluding remarks.

5.1 Optimal Control Method

We have developed an optimal control method in order to control the spectrum of the incompressible fluid flow. The method is based on the optimal control techniques. The cost functional is defined as an appropriate difference between the target and calculated energy spectra. This cost functional is minimized by a gradient based method. The gradient of the cost functional is obtained based on the solutions of the appropriate adjoint equation.

The particular interest in here is to discovering whether it is possible to produce the simultaneous dual cascades of energy and enstrophy and the corresponding scaling laws (i.e. $E \sim k^{-5/3}$ on the energy cascade and $E \sim k^{-3}$ on the enstrophy cascade) predicted by the classical KLB theory in a non-asymptotic sense. However, we emphasize that the method of controlling the energy spectrum of the flow introduced here can be used for other problems in fundamental turbulence research. For example, by making a particular choice of the weight function $w(t, k)$ in equation (3.6) one can control the rate at which an initially localized energy spectrum spreads over all scales. This can provide a different perspective to some problems such as transition to turbulence and drag (or lift) control in a flow over a rigid body which have already been studied through other approaches. Moreover, Gioia and Chakraborty [14] showed that the wall friction in a turbulent flow depends significantly on the energy spectrum of the flow. Therefore by controlling the energy spectrum one can also control the turbulent friction in pipe flow. The method could also be used in some benchmark studies in geophysical fluid dynamics. For instance, in a separate attempt (not published) we have produced the Gage–Nastrom spectrum [13] of mesoscale atmospheric flow in a forced two-

dimensional Navier-Stokes flow. Furthermore, our method could be modified easily to control the energy spectrum of geophysical fluid dynamics models such as the quasi-geostrophic and surface quasi-geostrophic equations.

5.2 Computations

Obtaining the gradient of the cost functional, requires solving an adjoint equation. In addition, the line-minimization (see §3.2.3) requires solving the Navier–Stokes equations several times. We have used a pseudo-spectral method with Krylove subspaces time integration to solve these equations.

In order to perform the optimization in a reasonable time, we have parallelized the NSE and adjoint equation solvers as described in §3.2.2. All computations are performed on the cluster `requin` of the SHARCNET facilities. The scaling analysis, shows almost linear speedup in most cases with efficiency close to 100%. This high efficiency is achieved thanks to the simple geometry of the problem together with the optimal structure of the code which minimizes the processor communications.

In our simulations 1024^2 number of grid points are used. The scaling analysis show that in this case, minimum computational time is achieved with an efficiency of almost 100% when 64 processors are used. Therefore, we have performed all computations on `requin` clusters with 64 processors.

5.3 Main Results

Our results demonstrate that when a full-band forcing is used (i.e. a forcing active over all scales), the KLB spectral slopes can be observed in a flow with a moderate Reynolds number. Such forcings clearly violate the inertial range assumption because some energy is directly injected by the external forcing into the wave-numbers of the scaling ranges. However, the inverse energy and forward enstrophy cascades still exist and their dynamics are dominated by the inertial interactions (i.e. triad interactions). This is similar to the linear forcing suggested by Lundgren [23] for numerical simulations of 3-D turbulence. Linear forcing is also full-band and therefore interferes with the inertial range dynamics. However, as we have found here for 2-D turbulence, Rosales and Meneveau [30] showed that the resulting statistical properties (e.g. stationarity and power-law scaling) of the flow under linear forcing are similar to the case where the conventional band-limited forcing active over largest scales is used.

Full-band forcings such as those considered here are of interest because they can be physically more realistic than band-limited forcings. Moreover, they are much easier to implement in numerical simulations which do not benefit from the scale selective property of spectral methods.

We also found that the optimal forcing automatically creates a sink of energy at largest scales. It has already been proved [7, 36, 34] in the case of monoscale forcing that such an infrared sink is a necessary condition in order to obtain the dual cascades and KLB scaling laws. We have observed a similar sink even when the forcing is full-band. Our result suggest the possibility to generalize the existing proofs to more general types of forcing.

In the case of band-limited forcing, the optimal control method still finds a forcing which results in the KLB scaling laws. However, the -3 range of the spectrum extends over only a quarter of a decade of wavenumbers. It is possible, however, to extend this scaling range by increasing the resolution (results not presented here).

Comparison of the energy spectra resulting from our optimal forcing and from the conventional random-phase band-limited forcing (figure 4.7) suggests that the details of the space-time structure of the forcing can crucially alter the statistical properties of the flow. For example figure 4.9 shows that the optimal forcing is particularly aligned in the favour of enstrophy injection. Replacing the phase-structure of the optimal forcing with a random variable (and preserving other properties of it) leads to a much steeper spectrum of the enstrophy cascade (i.e. $E \sim k^{-4}$). This shows that the conventional forcing (which is usually random in phase) has determining effects on the scaling properties of the enstrophy cascade.

On the other hand, small perturbations in the band-limited optimal forcing leads to a much steeper fall-off of the energy spectrum (close to k^{-4}). Moreover, we have not succeeded in constructing a simple model of the forcing based on the observed space-time properties of our optimal forcing. These observations imply that solutions of optimization problem (3.7) are quite sensitive to perturbations which is to be expected given the ill-posed character of the problem. This suggests that the optimal forcing belongings to a sparse set in the space of square-integrable band-limited functions. Therefore, it is quite unlikely to be physically realizable. This implies that reproducing the co-existing dual cascades which follow the KLB scaling laws is unlikely when a band-limited forcing is used with a moderate Reynolds number.

We would like to finish by suggesting some future research directions for this project.

1. Here, it was shown that a particular type of forcing can change the energy spectrum to an extent that the KLB prediction can be observed. However, the question to be investigated is: what is special about this forcing? We believe that a careful study of the alignments of the forcing with principle directions of the strain tensor (i.e. stretching and compression of the vorticity gradient) will answer this question and lead to a better

understanding of the dual cascade in two-dimensional turbulence.

2. Given the properties of the turbulent flow, one should ideally be able to fabricate a forcing which leads to the KLB energy spectrum without using the optimal control machinery. This will save a significant computational effort. A more detailed study of the optimal forcing is required in order to achieve this goal.

3. Finally, the optimal control method introduced here can be applied to study some fundamentals of turbulence such as study of drag/lift in a flow past a rigid body (as an alternative approach to the existing methods), turbulent friction control in a pipe flow and energy transfer in geophysical fluid flow.

Bibliography

[1] C. Basdevant, B. Legras, and R. Sadourny. A study of barotropic model flows: Intermittency, waves and predictability. *J. Atmos. Sci.*, 38:2305–2326, 1981.

[2] G. K. Batchelor. Computation of the energy spectrum in homogeneous two-dimensional turbulence. *Phys. Fluids Suppl.*, II:233–239, 1969.

[3] G. Boffetta. Energy and enstrophy fluxes in the double cascade of two-dimensional turbulence. *J. Fluid Mech.*, 589:253–260, 2007.

[4] G. Boffetta, A. Celani, S. Musacchio, and M. Vergassola. Intermittency in two-dimensional Ekman–Navier-Stokes turbulence. *Phys. Rev. E*, 66: 026304, 2002.

[5] V. Borue. Spectral exponents of enstrophy cascade in stationary two-dimensional homogeneous turbulence. *Phys. Rev. Lett.*, 71:3967, 1993.

[6] S. Chen, R. E. Ecke, G. L. Eyink, X. Wang, and Z. Xiao. Physical mechanism of the two-dimensional enstrophy cascade. *Phys. Rev. Lett.*, 91: 214501, 2003.

[7] P. Constantin, C. Foias, and O. Manley. Effects of the forcing function spectrum on energy spectrum in 2-D turbulence. *Phys. Fluids*, 6:427–429, 1994.

[8] W. S. Edwards, L. S. Tuckerman, R. A. Friesner, and D. C. Sorensen. Krylov methods for the incompressible Navier–Stokes equations. *J. Comp. Phys.*, 110:82–102, 1994.

[9] R. Fjørtoft. On the changes in the spectral distribution of kinetic energy for two dimensional, nondivergent flow. *Tellus*, 5:225–230, 1953.

[10] M. Frigo and S. G. Johnson. *FFTW user's manual*, 2003. URL `http://fftw.org/`.

[11] U. Frisch. *Turbulence: the legacy of A.N. Kolmogorov.* Cambridge University Press, 1995.

[12] U. Frisch and P. L. Sulem. Numerical simulation of inverse cascade in two-dimensional turbulence. *Phys. Fluids*, 27:1921–1923, 1984.

[13] K. S. Gage and G. D. Nastrom. On the spectrum of the atmospheric velocity fluctuations seen by mst/st radar and their interpretation. *Radio Sci.*, 20:1339–1374, 1985.

[14] G. Gioia and P. Chakraborty. Turbulent friction in rough pipes and the energy spectrum of the phenomenological theory. *Phys. Rev. Lett.*, 96: 044502, 2006.

[15] E. Gkioulekas and K. K. Tung. A new proof on net upscale energy cascade in two-dimensional and quasi-geostrophic turbulence. *J. Fluid Mech.*, 576: 173–189, 2007.

[16] M. Grasselli and D. Pelinovsky. *Numerical Mathematics.* Jones & Bartlett Publishers, 2008.

[17] A. K. Kolmogorov. The local structure of turbulence in incompressible viscous fluid for very large reynolds numbers. *Dokl. Akad. Nauk.*, 30: 301–305, 1941.

[18] R. H. Kraichnan. Inertial ranges in two-dimensional turbulence. *Phys. Fluids*, 10:1417–1423, 1967.

[19] R. H. Kraichnan. Inertial-ranges transfer in two- and three-dimensional turbulence. *J. Fluid Mech.*, 47:525–535, 1971.

[20] C. E. Leith. Diffusion approximation for two-dimensional turbulence. *Phys. Fluids*, 11:671–673, 1968.

[21] D. D. Lilly. Numerical simulation of two-dimensional turbulence. *Phys. Fluids Suppl.*, II:240–249, 1969.

[22] E. Lindborg and T. M. Alvelius. The kinetic energy spectrum of the two-dimensional enstrophy turbulence cascade. *Phys. Fluids*, 12:945, 2000.

[23] T. S. Lundgren. Linearly forced isotropic turbulence. Technical report, Center for Turbulence Research, 2003.

[24] M. E. Maltrud and G. K. Vallis. Energy and enstrophy transfer in numerical simulations of two-dimensional turbulence. *Phys. Fluids A*, 5: 1760–1775, 1993.

[25] P. C. Martin and C. D. Dominicis. The long distance behavior of randomly stirred fluids. *Prog. Theor. Phys. Suppl.*, 64:108–123, 1978.

[26] P. E. Merilees and H. Warn. On energy and enstrophy exchanges in two-dimensional non-divergent flow. *J. Fluid Mech.*, 69:625–630, 1975.

[27] J. Nocedal and S. J. Wright. *Numerical Optimization.* Springer, 2000.

[28] C. Pasquero and G. Falkovich. Stationary spectrum of vorticity cascade in two-dimensional turbulence. *Phys. Rev. E*, 65:056305, 2002.

[29] B. Protas, T. R. Bewley, and G. Hagen. A comprehensive framework for the regularization of adjoint analysis in multiscale PDE systems. *J. Comp. Phys.*, 195:49–89, 2004.

[30] C. Rosales and C. Meneveau. Linear forcing in numerical simulations of isotropic turbulence: Physical space implementation and convergence studies. *Phys. Fluids*, 17:095106, 2005.

[31] N. Schorghofer. Energy spectra of steady two-dimensional turbulent flows. *Phys. Rev. E*, 61:6575–6577, 2000.

[32] J. C. Schulze and P. J. Schmid J. L. Sesterhenn. Exponential time integration using Krylov subspaces. *Int. J. Numer. Meth. Fluids*, 60:591–609, 2009.

[33] L. M. Smith and V. Yakhot. Bose condensation and small-scale structure generation in a random force driven 2d turbulence. *Phys. Rev. Lett.*, 71: 352–355, 1993.

[34] C. V. Tran and J. C. Bowman. On the dual cascade in two dimensional turbulence. *Physica D*, 176:242–255, 2003.

[35] C. V. Tran and D. G. Dritschel. Vanishing enstrophy dissipation in two-dimensional Navier–Stokes turbulence in the inviscid limit. *J. Fluid Mech.*, 559:107–116, 2006.

[36] C. V. Tran and T. G. Shepherd. Constraints on the spectral distribution of energy and enstrophy dissipation in forced two-dimensional turbulence. *Physica D*, 165:199–212, 2002.

[37] C. V. Tran, D. G. Dritschel, and R. K. Scott. Revisiting batchelor's theory of two-dimensional turbulence. *J. Fluid Mech.*, 591:379–391, 2007.

[38] Y.-K. Tsang and W. R. Young. Force-dissipative two-dimensional turbulence: A scaling regime controlled by drag. *Phys. Rev. E*, 79:045308(R), 2009.

[39] Y.-K. Tsang, E. Ott, T. M. Antonsen, and P. N. Guzdar. Intermittency in two-dimensional turbulence with drag. *Phys. Rev. E*, 71:066313, 2005.

[40] W. T. Vetterling, S. A. Teukolsky, W. H. Press, and B. P. Flannery. *Numerical Recipes.* Cambrige University Press, 2007.

[41] W. T. Welch and K. K. Tung. Nonlinear baroclinic adjustment and wavenumber selection in a simple case. *J. Atmos. Sci.*, 55:1285–1302, 1998.

[42] V. Yakhot. Universal stirring force in the theory of isotropic turbulence. *Phys. Rev. A*, 24:3268–3271, 1981.

Index